SN 2020bvc: A Broad-line Type Ic Supernova with a Double-peaked Optical Light Curve and a Luminous X-Ray and Radio Counterpart

Anna Y. Q. Ho[1], S. R. Kulkarni[1], Daniel A. Perley[2], S. Bradley Cenko[3,4], Alessandra Corsi[5], Steve Schulze[6], Ragnhild Lunnan[7], Jesper Sollerman[7], Avishay Gal-Yam[6], Shreya Anand[8], Cristina Barbarino[7], Eric C. Bellm[9], Rachel J. Bruch[10], Eric Burns[11,12], Kishalay De[1], Richard Dekany[13], Alexandre Delacroix[13], Dmitry A. Duev[1], Dmitry D. Frederiks[14], Christoffer Fremling[1], Daniel A. Goldstein[1,22], V. Zach Golkhou[9,15,23], Matthew J. Graham[1], David Hale[13], Mansi M. Kasliwal[1], Thomas Kupfer[16], Russ R. Laher[17], Julia Martikainen[18,19], Frank J. Masci[17], James D. Neill[1], Anna Ridnaia[14], Ben Rusholme[17], Volodymyr Savchenko[20], David L. Shupe[17], Maayane T. Soumagnac[10,21], Nora L. Strotjohann[6], Dmitry S. Svinkin[14], Kirsty Taggart[2], Leonardo Tartaglia[7], Lin Yan[13], and Jeffry Zolkower[13]

[1] Cahill Center for Astrophysics, California Institute of Technology, MC 249-17, 1200 East California Boulevard, Pasadena, CA 91125, USA
[2] Astrophysics Research Institute, Liverpool John Moores University, IC2, Liverpool Science Park, 146 Brownlow Hill, Liverpool L3 5RF, UK
[3] Astrophysics Science Division, NASA Goddard Space Flight Center, Mail Code 661, Greenbelt, MD 20771, USA
[4] Joint Space-Science Institute, University of Maryland, College Park, MD 20742, USA
[5] Department of Physics and Astronomy, Texas Tech University, Box 1051, Lubbock, TX 79409-1051, USA
[6] Department of Particle Physics and Astrophysics, Weizmann Institute of Science, 234 Herzl Street, Rehovot 76100, Israel
[7] The Oskar Klein Centre & Department of Astronomy, Stockholm University, AlbaNova, SE-106 91 Stockholm, Sweden
[8] Division of Physics, Mathematics, and Astronomy, California Institute of Technology, Pasadena, CA 91125, USA
[9] DIRAC Institute, Department of Astronomy, University of Washington, 3910 15th Avenue NE, Seattle, WA 98195, USA
[10] Department of Particle Physics and Astrophysics, Weizmann Institute of Science, Rehovot 76100, Israel
[11] NASA Postdoctoral Program Fellow, Goddard Space Flight Center, Greenbelt, MD 20771, USA
[12] Department of Physics & Astronomy, Louisiana State University, Baton Rouge, LA 70803, USA
[13] Caltech Optical Observatories, California Institute of Technology, Pasadena, CA 91125, USA
[14] Ioffe Institute, Politekhnicheskaya 26, St. Petersburg 194021, Russia
[15] The eScience Institute, University of Washington, Seattle, WA 98195, USA
[16] Kavli Institute for Theoretical Physics, University of California, Santa Barbara, CA 93106, USA
[17] IPAC, California Institute of Technology, 1200 East California Boulevard, Pasadena, CA 91125, USA
[18] Department of Physics, University of Helsinki, P.O. Box 64, FI-00014, Finland
[19] Nordic Optical Telescope, Roque de Los Muchachos Observatory, Rambla José Ana Fernández Pérez 7, E-38711 Breña Baja, La Palma, Canarias, Spain
[20] ISDC, Department of Astronomy, University of Geneva, Chemin d'Ecogia, 16 CH-1290 Versoix, Switzerland
[21] Lawrence Berkeley National Laboratory, 1 Cyclotron Road, Berkeley, CA 94720, USA

Abstract

We present optical, radio, and X-ray observations of SN 2020bvc (=ASASSN-20bs, ZTF 20aalxlis), a nearby ($z = 0.0252$; $d = 114$ Mpc) broad-line (BL) Type Ic supernova (SN) and the first double-peaked Ic-BL discovered without a gamma-ray burst (GRB) trigger. Our observations show that SN 2020bvc shares several properties in common with the Ic-BL SN 2006aj, which was associated with the low-luminosity gamma-ray burst (LLGRB) 060218. First, the 10 GHz radio luminosity ($L_{\rm radio} \approx 10^{37}$ erg s^{-1}) is brighter than ordinary core-collapse SNe but fainter than LLGRB SNe such as SN 1998bw (associated with LLGRB 980425). We model our VLA observations (spanning 13–43 days) as synchrotron emission from a mildly relativistic ($v \gtrsim 0.3c$) forward shock. Second, with Swift and Chandra, we detect X-ray emission ($L_X \approx 10^{41}$ erg s^{-1}) that is not naturally explained as inverse Compton emission or part of the same synchrotron spectrum as the radio emission. Third, high-cadence ($6\times$ night^{-1}) data from the Zwicky Transient Facility (ZTF) show a double-peaked optical light curve, the first peak from shock cooling of extended low-mass material (mass $M_e < 10^{-2}\,M_\odot$ at radius $R_e > 10^{12}$ cm) and the second peak from the radioactive decay of ^{56}Ni. SN 2020bvc is the first double-peaked Ic-BL SN discovered without a GRB trigger, so it is noteworthy that it shows X-ray and radio emission similar to LLGRB SNe. For four of the five other nearby ($z \lesssim 0.05$) Ic-BL SNe with ZTF high-cadence data, we rule out a first peak like that seen in SN 2006aj and SN 2020bvc, i.e., that lasts ≈ 1 day and reaches a peak luminosity $M \approx -18$. Follow-up X-ray and radio observations of Ic-BL SNe with well-sampled early optical light curves will establish whether double-peaked optical light curves are indeed predictive of LLGRB-like X-ray and radio emission.

Supporting material: data behind figure, machine-readable table

---

[22] Hubble Fellow.
[23] Moore-Sloan, WRF Innovation in Data Science, and DIRAC Fellow.

1. Introduction

It is well established that most long-duration gamma-ray bursts (GRBs) arise from massive-star explosions (see Woosley & Bloom 2006 for a detailed review, and Hjorth & Bloom 2012 and Cano et al. 2017 for recent updates). The traditional model (reviewed in Piran 2004) is that a massive star, stripped of its hydrogen and helium envelopes, collapses and forms a black hole or neutron star. Through rotational spin-down or accretion, the newborn compact object launches an outflow that tunnels through the star, breaks out from the surface as a narrowly collimated jet, and appears as a GRB when viewed on axis from Earth. The jet shocks the circumburst medium, producing a long-lived "afterglow" across the electromagnetic spectrum. The same "central engine" that launches the GRB also unbinds the stellar material in a supernova (SN) that has a greater kinetic energy (10^{52} erg) and photospheric velocity ($\gtrsim 20{,}000 \, \text{km s}^{-1}$) than ordinary core-collapse SNe (Sobacchi et al. 2017; Barnes et al. 2018). These high-velocity, high-energy SNe were originally called "hypernovae" (e.g., Iwamoto et al. 1998), but a more common term today is "broad-line Type Ic" (Ic-BL) SNe (Gal-Yam 2017).

Thousands of GRBs have been discovered, with hundreds of afterglows and a dozen Ic-BL SNe (GRB SNe) identified in follow-up observations. Half of the known GRB SNe are associated with low-luminosity GRBs (LLGRBs), defined as having an isotropic gamma-ray luminosity of $L_{\gamma,\text{iso}} < 10^{48.5} \, \text{erg s}^{-1}$ rather than the $L_{\gamma,\text{iso}} > 10^{49.5} \, \text{erg s}^{-1}$ of cosmological GRBs (Hjorth 2013; Cano et al. 2017). Although LLGRBs are 10–100 times more common than cosmological GRBs (Soderberg et al. 2006; Liang et al. 2007), the discovery rate by GRB detectors is much lower (one every few years) due to the small volume in which they can be detected. So, the sample size remains small, and the connection between classical GRBs, LLGRBs, and Ic-BL SNe remains unknown.

To make progress on understanding the GRB-LLGRB-SN connection, wide-field high-cadence optical surveys can be used in conjunction with radio and X-ray follow-up observations to discover GRB-related phenomena without relying on a GRB trigger (e.g., Soderberg et al. 2010; Cenko et al. 2013; Margutti et al. 2014; Corsi et al. 2017). To this end, for the past 2 yr, we have been conducting a systematic search for engine-driven explosions using the high cadence ($6\times \, \text{night}^{-1}$) and nightly cadence ($2\times \, \text{night}^{-1}$) surveys of the Zwicky Transient Facility (ZTF; Bellm et al. 2019b; Graham et al. 2019), which have a combined area of 5000 deg^2 (Bellm et al. 2019a).

Here we present the most recent event detected as part of the ZTF engine-driven SN program: SN 2020bvc (=ASASSN-20bs) was first reported to the Transient Name Server (TNS[24]) by the All-Sky Automated Survey for SuperNovae (ASAS-SN; Shappee et al. 2014), and the discovery announcement noted the rapid rise and likely core collapse (CC) SN origin (Stanek 2020). It was also reported by the Asteroid Terrestrial-impact Last Alert System (ATLAS; Tonry et al. 2018) as ATLAS20feh (on February 5.61). The first detection of SN 2020bvc was in ZTF high-cadence data on February 4.34. We classified the event as a Ic-BL SN (Perley et al. 2020), and the high-cadence data showed a double-peaked light curve. Recognizing the similarity to the Ic-BL SN 2006aj associated with LLGRB 060218 (Ferrero et al. 2006; Mirabal et al. 2006; Pian et al. 2006; Soderberg et al. 2006; Sollerman et al. 2006),

we triggered X-ray and radio (Ho et al. 2020a) follow-up observations.

This paper is structured as follows. We present our observations of SN 2020bvc in Section 2. In Section 3 we measure basic light-curve properties and the blackbody evolution. In Section 4 we discuss the evolution of the optical spectra. In Section 5 we show that the optical light curve can be explained as a combination of shock-cooling emission from extended low-mass material ($M_e < 10^{-2} \, M_\odot$ at $R_e > 10^{12}$ cm) and radioactive decay of ^{56}Ni. In Section 6 we model the forward shock and show that the radio emission can be explained with velocities that are only mildly relativistic. In Section 7 we show ZTF light curves of five other nearby ($z < 0.05$) Ic-BL SNe in the high-cadence surveys and rule out a luminous first peak like that seen in SN 2006aj and SN 2020bvc for four events. We conclude in Section 8 by summarizing the properties of SN 2020bvc and discussing its implications for the GRB-LLGRB-SN connection.

2. Observations

2.1. ZTF Detection and Classification

On 2020 February 4.34,[25] SN2020bvc was detected at $i = 17.48 \pm 0.05$ mag[26] at $\alpha = 14^{\text{h}}33^{\text{m}}57\overset{\text{s}}{.}01$, $\delta = +40^{\text{d}}14^{\text{m}}37\overset{\text{s}}{.}5$ (J2000) as part of the ZTF Uniform Depth Survey[27] (ZUDS; D. A. Goldstein et al. 2020, in preparation) with the 48 inch Samuel Oschin Schmidt telescope at Palomar Observatory (P48). The ZTF observing system is described in Dekany et al. (2020). The identification of SN 2020bvc made use of machine learning–based real–bogus classifiers (Duev et al. 2019; Mahabal et al. 2019) and a star–galaxy separator (Tachibana & Miller 2018).

The last nondetection by ZTF was 1.78 days prior to the first detection ($r > 20.67$ mag), with more recent limits from ATLAS (0.67 days, o-band > 19.4 mag) and ASASSN (0.74 days, $g > 18.6$ mag). Throughout the paper, we use the time of the ATLAS nondetection (February 3.67) as our reference epoch, t_0. Our estimate of the "epoch of first light," t_0, is supported by aligning the light curves of SN 2020bvc and SN 2006aj, discussed in Section 3.1.

Two hours after the first detection, we obtained a spectrum using the Spectral Energy Distribution Machine (SEDM; Blagorodnova et al. 2018; Rigault et al. 2019), a low-resolution spectrograph on the automated 60 inch telescope at Palomar Observatory (P60; Cenko et al. 2006). The spectrum is dominated by a thermal continuum with hydrogen emission lines from the host galaxy and possible weak absorption features that we discuss in Section 4. On February 8.24, a spectrum we obtained using the Spectrograph for the Rapid Acquisition of Transients (SPRAT; Piascik et al. 2014) on the Liverpool Telescope (LT; Steele et al. 2004) showed features consistent with a Ic-BL SN (Perley et al. 2020). We discuss the spectroscopic evolution of SN 2020bvc in Section 4. Follow-up observations were coordinated through the GROWTH Marshal (Kasliwal et al. 2019), and the optical photometry and spectroscopy will be made public through the Weizmann Interactive Supernova Data Repository (WISeREP; Yaron & Gal-Yam 2012).

---

[24] https://wis-tns.weizmann.ac.il/

[25] All times given in UTC.
[26] All magnitudes given in AB.
[27] Forty-five fields (2000 deg^2) twice per night in each of the g, r, and i bands.
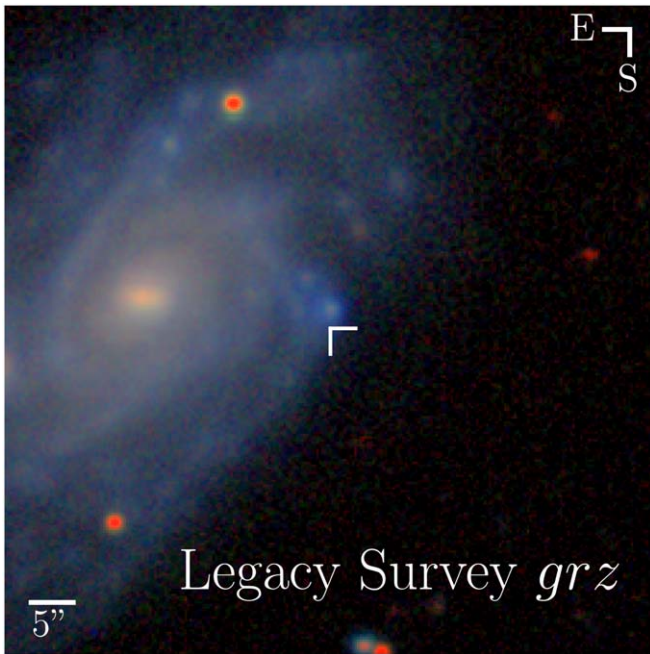
Figure 1. Position of SN 2020bvc (white crosshairs) in its host galaxy UGC 09379. The *g*-, *r*-, and *z*-band images from the DESI Legacy Survey (Dey et al. 2019) were combined using the prescription in Lupton et al. (2004).

2.2. Host Galaxy

The position of SN 2020bvc is $13''$ (7.2 kpc[28]) from the center of UGC 09379 ($z = 0.025201 \pm 0.000021$ from NED[29]), which also hosted PTF 13ast (Gal-Yam et al. 2014). The galaxy UGC 09379 is massive; Chang et al. (2015) estimated a stellar mass $\log_{10}(M/M_\odot) = 10.28^{+0.01}_{-0.16}$, while the NASA-SDSS Atlas value (Blanton et al. 2011) is $\log_{10}(M/M_\odot) = 10.26$, comparable to the Milky Way and other large spirals. The stellar mass of UGC 09379 is larger than that of all known GRB SN host galaxies (Hjorth & Bloom 2012; Taggart & Perley 2019) and similar only to the host galaxy of LLGRB 171205A/SN 2017iuk (D'Elia et al. 2018; Wang et al. 2018; Izzo et al. 2019), which had $\log_{10}(M/M_\odot) = 10.1 \pm 0.1$ (Perley & Taggart 2017). The stellar mass of UGC 09379 is also larger than that of most Ic-BL SN host galaxies (Modjaz et al. 2020), with the exception of SN 2002ap[30] and SN 1997ef[31].

As shown in Figure 1, SN 2020bvc is $1''\!.46 \pm 0''\!.34$ (804 ± 187 pc) from a bright H II region. We leave a detailed analysis of the SN site to future work but note that two nearby LLGRB SNe, LLGRB 980425/SN 1998bw (Galama et al. 1998; Kulkarni et al. 1998) and LLGRB 020903 (Sakamoto et al. 2004; Soderberg et al. 2004; Bersier et al. 2006), were located 800 and 460 pc, respectively, from similar bright compact regions in the outskirts of their host galaxies (Sollerman et al. 2005; Hammer et al. 2006). Because these events took place outside the nearest massive-star cluster, it has been argued that the progenitors were Wolf–Rayet stars ejected from the cluster (Hammer et al. 2006; Cantiello et al. 2007; Eldridge et al. 2011; van den Heuvel & Portegies Zwart 2013).

We also note that the metallicity of the SN site is quite low (we infer $12 + \log[\mathrm{O/H}] = 8.2$ from the underlying nebular emission in our March 22 Low Resolution Imaging Spectrometer (LRIS) spectrum using the N2 diagnostic from Pettini & Pagel 2004), making the appearance of an SN of this type in such a massive galaxy less surprising. This metallicity estimate is consistent with the measurement of Izzo et al. (2020).

2.3. Optical Photometry

As shown in Figure 2, SN 2020bvc was observed almost nightly in *gri* by the P48 for the first month postexplosion. We obtained additional *ugriz* and *gri* photometry using the IO:O on the LT and the SEDM on the P60, respectively. The pipeline for P48 photometry is described in Masci et al. (2019) and makes use of the image-subtraction method of Zackay et al. (2016). The LT image reduction was provided by the basic IO:O pipeline. The P60 and LT image subtraction were performed following Fremling et al. (2016) using PS1 images for *griz* and the Sloan Digital Sky Survey (SDSS) for the *u* band. Values were corrected for Milky Way extinction following Schlafly & Finkbeiner (2011) with $E(B - V) = A_V/R_V = 0.034$ mag using $R_V = 3.1$ and a Fitzpatrick (1999) extinction law. The full set of photometry is provided in Table A1 in Appendix A and plotted in Figure 3.

2.4. Spectroscopy

We obtained 13 ground-based optical spectra using the SEDM, the Andalusia Faint Object Spectrograph and Camera (ALFOSC[32]) on the Nordic Optical Telescope (NOT; Djupvik & Andersen 2010), the Double Beam Spectrograph (DBSP; Oke & Gunn 1982) on the 200 inch Hale telescope at Palomar Observatory, SPRAT on the LT, and the LRIS (Oke et al. 1995) on the Keck I 10 m telescope. The SEDM pipeline is described in Rigault et al. (2019), the SPRAT pipeline is based on the FrodoSpec pipeline (Barnsley et al. 2012), the P200/ DBSP pipeline is described in Bellm & Sesar (2016), and the Keck/LRIS pipeline `Lpipe` is described in Perley (2019).

Epochs of spectroscopic observations are marked with an "S" in Figure 2, and observation details are provided in Table 1. The spectral sequence is shown in Figure 4 and discussed in more detail in Section 4. Both raw and smoothed versions of the spectra will be made available on WISeREP.

2.5. UV and X-Ray Observations

We obtained 10 observations of SN 2020bvc[33] with the Ultraviolet/Optical Telescope (UVOT; Roming et al. 2005) and X-Ray Telescope (XRT; Burrows et al. 2005) on board the Neil Gehrels Swift Observatory (Gehrels et al. 2004) under a target-of-opportunity program (PI: Schulze). The first observation was on February 5.02 ($\Delta t = 1.35$). We also obtained two 10 ks observations with the Chandra X-ray Observatory under Director's Discretionary Time (PI: A. Ho), one epoch on February 16[34] ($\Delta t = 13.2$) and one epoch on February 29[35] ($\Delta t = 25.4$).

---

[28] ΛCDM cosmology of Planck Collaboration et al. (2016) used throughout.
[29] ned.ipac.caltech.edu
[30] M74: $\log_{10}(M/M_\odot) = 11.52^{+0.05}_{-0.05}$ (Kelly & Kirshner 2012).
[31] UGC 4107: $\log_{10}(M/M_\odot) = 10.55^{+0.07}_{-0.56}$ (Kelly & Kirshner 2012).

[32] http://www.not.iac.es/instruments/alfosc/
[33] The target name was PTF 13ast, a previous SN hosted by UGC 09379.
[34] ObsID 23171, data set [ADS/Sa.CXO#obs/23171].
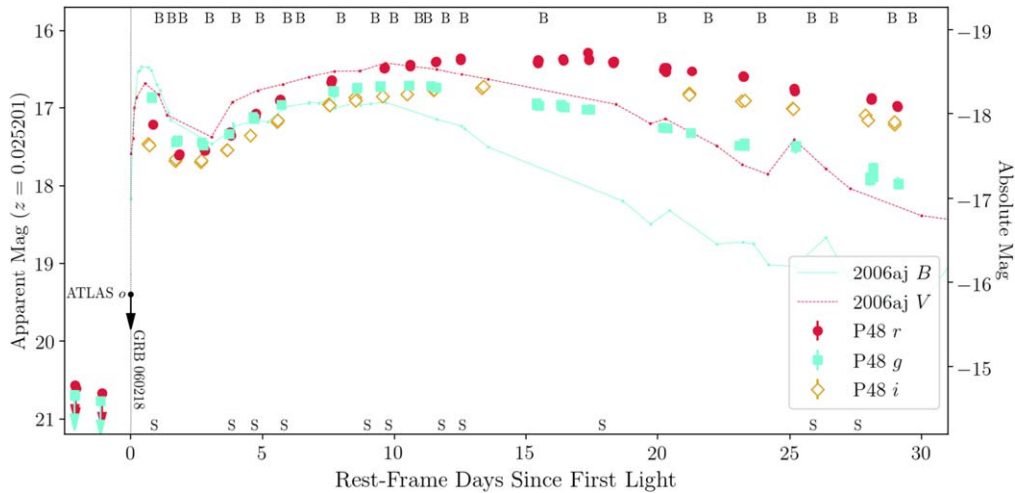[35] ObsID 23172, data set [ADS/Sa.CXO#obs/23172].

Figure 2. The *g*-, *r*-, and *i*-band light curves of SN 2020bvc from ZUDS and an upper limit from ATLAS. Measurements have been corrected for Milky Way extinction. Epochs of follow-up spectroscopy are indicated with an "S" along the bottom of the figure. Epochs of blackbody fits (Section 3.2) are indicated with a "B" along the top of the figure. For comparison, we show the *B*- and *V*-band light curves of SN 2006aj ($z = 0.033$) transformed to the redshift of SN 2020bvc ($z = 0.025201$). The SN 2006aj light curve was taken from the Open Supernova Catalog and corrected for Milky Way extinction; the data are originally from Modjaz et al. (2006), Bianco et al. (2014), and Brown et al. (2014). We indicate the relative time of LLGRB 060218 compared to the light curve of SN 2006aj.

The UVOT photometry was performed using the task `UVOTsource` in HEASoft[36] version 6.25 (Blackburn et al. 1999) with a 3″ radius aperture. For host subtraction, a template was constructed from data prior to 2014 December 9. Host-subtracted, Milky Way extinction–corrected values are provided in Table A1 in Appendix A. The XRT data were reduced using the online tool[37] from the Swift team (Evans et al. 2007, 2009) with the data binned by observation and centroiding turned off. Chandra data were reduced using the Chandra Interactive Analysis of Observations (CIAO) software package (v4.12; Fruscione et al. 2006).

Stacking the first 2.2 ks of XRT observations (four nightly 0.6 ks exposures), we detected four counts with an expected background of 0.16 counts. The resulting count rate is $(2.9^{+3.3}_{-1.9}) \times 10^{-3}$ s^{-1} (90% confidence interval). To convert count rate to flux, we used a hydrogen column density $n_H = 9.90 \times 10^{19}$ cm^{-2} (HI4PI Collaboration et al. 2016) and a photon power-law index of $\Gamma = 2$. The resulting unabsorbed 0.3–10 keV flux is $(9.3^{+10.6}_{-6.1}) \times 10^{-14}$ erg s^{-1} cm^{-2}, and the luminosity is $(1.4^{+1.7}_{-0.9}) \times 10^{41}$ erg s^{-1}. From prior Swift observations of the position of SN 2020bvc, we measured a 90% upper limit of $<7.8 \times 10^{-4}$ s^{-1}, suggesting that the emission is not from the host. We note that there is a discrepancy between our Swift measurements and those in Izzo et al. (2020), who found a significantly higher XRT flux value.

In the first epoch of our Chandra observations, a total of eight counts were detected in a 1″ radius region centered on the source. To measure the background, we set an annulus around the source with an inner radius of 3″ and an outer radius of 10″. The average background was 0.″21^{-2}, so the expected number of background counts within the source region is 0.65. The 90% confidence interval for the number of detected counts from the source is 3.67–13.16 (Kraft et al. 1991), so we conclude that the detection is significant.

We used CIAO to convert the count rate from the first observation ($(5.9^{+5.1}_{-3.3}) \times 10^{-4}$ s^{-1}) to flux, assuming the same photon index and n_H value as for the Swift observations,

finding an unabsorbed 0.5–7 keV flux of $(7.2^{+6.3}_{-3.9}) \times 10^{-15}$ erg s^{-1} cm^{-2}. In the second epoch, seven counts were detected, with a count rate of $(5.9^{+5.1}_{-3.2}) \times 10^{-4}$ s^{-1} and an unabsorbed 0.5–7 keV flux of $(7.2^{+6.2}_{-4.0}) \times 10^{-15}$ erg s^{-1} cm^{-2}. The corresponding luminosity is $(1.1^{+1.0}_{-0.6}) \times 10^{40}$ erg s^{-1} in each epoch. In Section 6.2 we compare the X-ray light curve to that of other Ic-BL SNe. Again, we note a discrepancy with the measurements of Izzo et al. (2020), who found a significantly higher flux value than we did (as shown in their Figure 2).

2.6. Submillimeter and Radio Observations

As listed in Table 2, we obtained eight observations of SN 2020bvc[38] with the Karl G. Jansky Very Large Array (VLA; Perley et al. 2011) while the array was in C configuration. We used 3C 286 as the flux density and bandpass calibrator and J1417+4607 as the complex gain calibrator. The data were calibrated using the automated pipeline available in the Common Astronomy Software Applications (CASA; McMullin et al. 2007), with additional flagging performed manually, and imaged[39] using the CLEAN algorithm (Högbom 1974).

Motivated by the detection of LLGRB 980425/SN 1998bw (Galama et al. 1998) at 2 mm (Kulkarni et al. 1998) and LLGRB 171205A/SN 2017iuk at 3 and 1 mm (Perley et al. 2017), we also observed[40] SN 2020bvc with the Submillimeter Array (SMA; Ho et al. 2004), which was in its compact configuration.[41] The phase and amplitude gain calibrators were J1419+383 and J1310+323, the passband calibrator was 3C 84, and the flux calibrator was Uranus. Data were calibrated

---

[36] http://heasarc.gsfc.nasa.gov/ftools
[37] https://www.swift.ac.uk/user_objects/

[38] Program VLA/20A-374; PI: A. Ho.
[39] Cell size was 1/10 of the synthesized beamwidth, and field size was the smallest magic number (10×2^n) larger than the number of cells needed to cover the primary beam.
[40] Program 2019B-S026; PI: A. Ho.
[41] The RxA and RxB receivers were tuned to a local oscillator frequency of 223.556 GHz, providing 16 GHz of overlapping bandwidth: 211.56–219.56 GHz in the lower sideband and 227.56–235.56 GHz in the upper sideband with a spectral resolution of 140.0 kHz channel^{-1}.
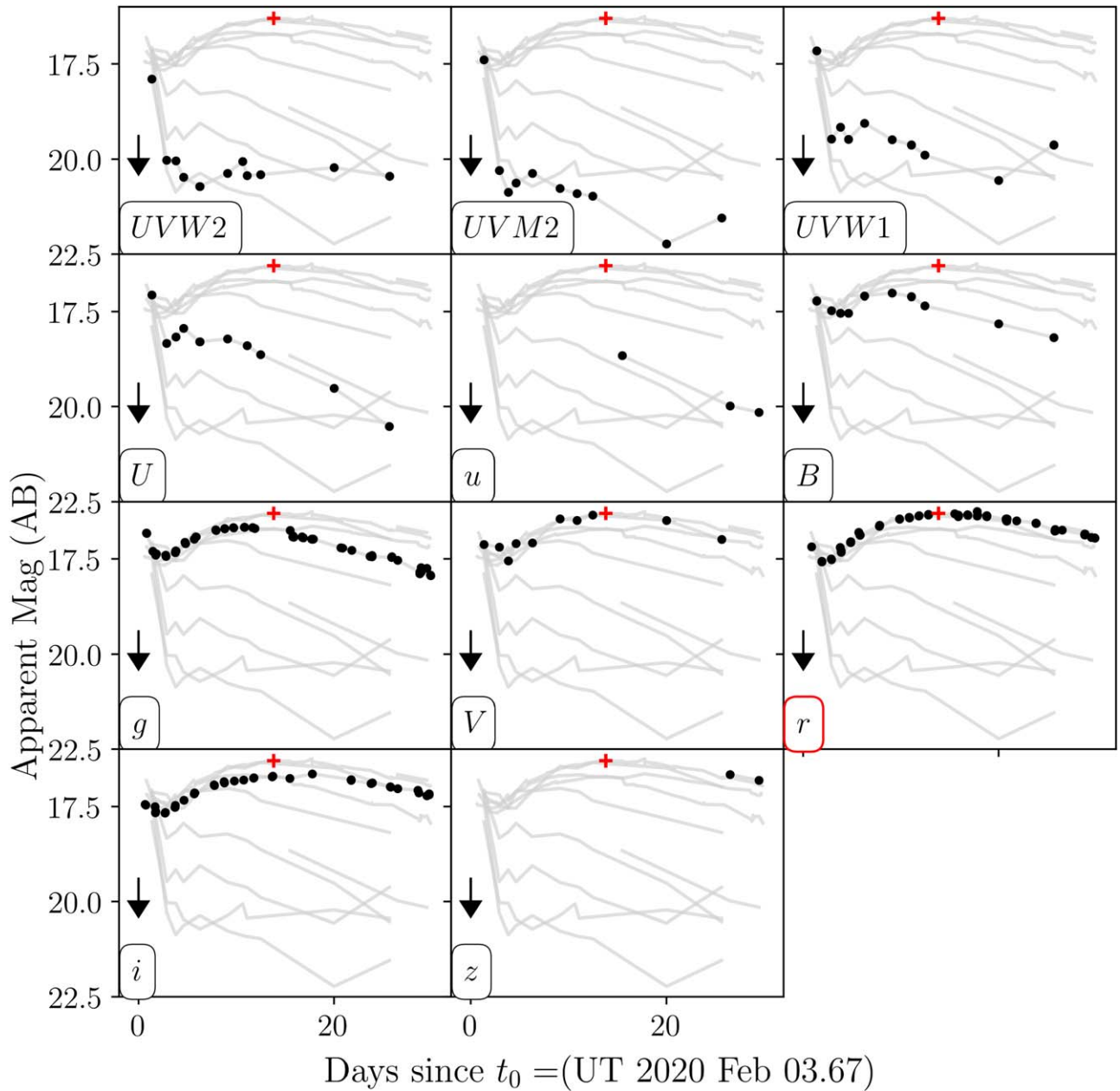
Figure 3. UV and optical light curves of SN 2020bvc from Swift and ground-based facilities. The arrow marks the last upper limit, which was by ATLAS in the o-band. The red plus sign marks the peak of the r-band light curve. The full set of light curves is shown as gray lines in the background, and each panel highlights an individual filter in black.

using the SMA MIR IDL package and imaged using MIRIAD (Sault et al. 1995).

No source was detected by the SMA with a spectral channel-averaged 1σ rms of 0.25 mJy. A source was detected at the position of SN 2020bvc in all epochs of VLA observation, and no sources were detected elsewhere in the host galaxy. Using the task imfit, we confirm that the radio source is a point source at all frequencies, and that the centroid is at the position of the optical transient. In Figure 5, we show the centroid of the radio emission and the position of the optical transient and that both are offset from the nearby H II region.

In the first observation ($\Delta t = 13$ days), the 10 GHz peak flux density was $63 \pm 6\,\mu$Jy, corresponding to a luminosity of 1.0×10^{27} erg s^{-1} Hz^{-1} (Ho 2020). The source was brighter at lower frequencies, and there is marginal (2σ) evidence for fading at 6 ($F_\nu \propto t^{-0.23 \pm 0.15}$) and 10 ($F_\nu \propto t^{-0.25 \pm 0.16}$) GHz but

no evidence for fading at 3 GHz. The radio SED is shown in Figure 6. In Section 6 we compare the 10 GHz light curve to that of other Ic-BL SNe and use the SED to model the forward shock.

2.7. Search for a GRB

The third Interplanetary Network (IPN[42]) consists of six spacecraft that provide all-sky full-time monitoring for high-energy bursts. The most sensitive detectors in the IPN are the Swift Burst Alert Telescope (BAT; Barthelmy et al. 2005) the Fermi Gamma-ray Burst Monitor (GBM; Meegan et al. 2009), and the Konus instrument on the WIND spacecraft (Aptekar et al. 1995).
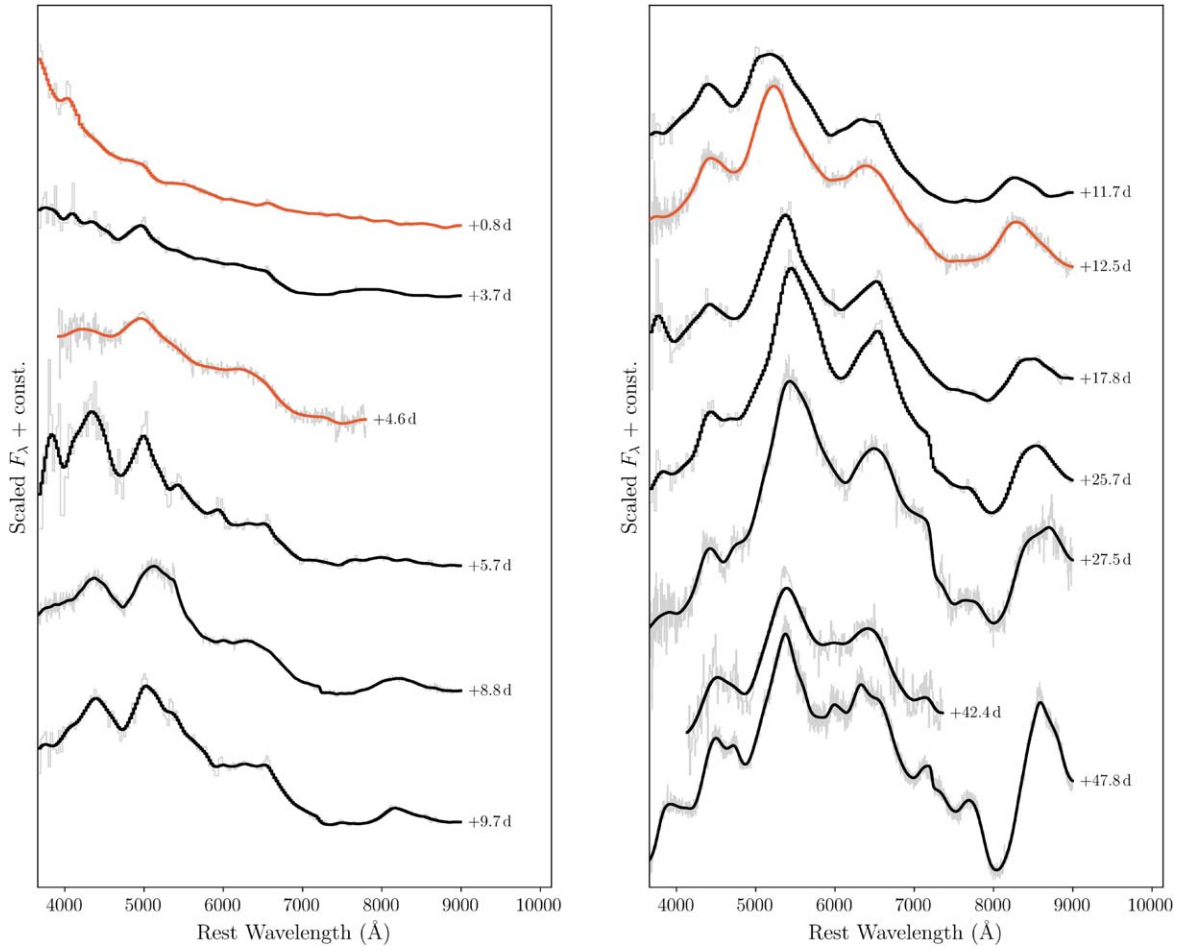
---

[42] http://ssl.berkeley.edu/ipn3/index.html

Figure 4. Optical spectra of SN 2020bvc. The phase is relative to t_0, defined in Section 2.1 as the time of the last nondetection by ATLAS. The first spectrum is dominated by a blue continuum. By $\Delta t = 5.7$ days, the spectrum strongly resembles a Ic-BL SN. The raw spectrum is shown in light gray, and a smoothed spectrum (with host emission lines removed) is overlaid in black. Spectra highlighted in orange are plotted compared to LLGRB SNe at similar phases in Figure 10.

(The data used to create this figure are available.)

Table 1
Spectroscopic Observations of SN 2020bvc

Date (UTC)	Δt (days)	Tel.+Instr.	Exp. Time (s)	v_{ph} (10^4 km s^{-1})
Feb 4.43	0.76	P60+SEDM	1800	...
Feb 7.36	3.7	P60+SEDM	1800	5.1 ± 0.1
Feb 8.24	4.6	LT+SPRAT	600	2.58 ± 0.51
Feb 9.36	5.7	P60+SEDM	1800	...
Feb 12.51	8.8	P200+DBSP	600	1.83 ± 0.32
Feb 13.33	9.7	P60+SEDM	1800	...
Feb 15.33	11.7	P60+SEDM	1800	...
Feb 16.14	12.5	NOT+ALFOSC	1200	1.90 ± 0.25
Feb 21.43	17.7	P60+SEDM	1800	...
Feb 29.42	25.8	P60+SEDM	1800	...
Mar 2.14	27.5	NOT+ALFOSC	1200	...
Mar 17.19	42.6	LT+SPRAT	900	1.72 ± 0.32
Mar 22.50	47.9	Keck I+LRIS	300	1.79 ± 0.39

Note. Epochs given since t_0 as defined in Section 2.1. Velocities are derived from Fe II absorption features as described in Section 4.2.

We searched the Fermi GBM Burst Catalog[43] (Gruber et al. 2014; von Kienlin et al. 2014; Narayana Bhat et al. 2016), the

Table 2
Submillimeter- and Centimeter-wavelength Radio Observations of SN 2020bvc

Start Date (UTC)	Time on-source (hr)	Δt (days)	ν (GHz)	Flux Density (μJy)
Feb 9.42	4.7	5.8	230	<250
Feb 16.67	0.4	13.0	10	63 ± 6
Feb 20.64	0.4	17.0	6	83 ± 6
Feb 27.64	0.4	24.0	3	111 ± 10
Mar 2.63	0.4	28.0	15	33 ± 4
Mar 9.60	0.4	35.0	10	50 ± 5
Mar 13.59	0.4	39.0	3	106 ± 10
Mar 17.33	0.4	42.7	6	63 ± 6

Note. The 230 GHz measurement was obtained using the SMA (upper limit given as 1σ rms), and the lower-frequency measurements were obtained using the VLA.

Fermi-GBM Subthreshold Trigger list[44] (with reliability flag ! = 2), the Swift GRB Archive,[45] the IPN master list,[46] and the

---
[43] https://heasarc.gsfc.nasa.gov/W3Browse/fermi/fermigbrst.html

[44] https://gcn.gsfc.nasa.gov/fermi_gbm_subthresh_archive.html
[45] https://swift.gsfc.nasa.gov/archive/grb_table/
[46] http://ipn3.ssl.berkeley.edu/masterli.txt

Gamma-Ray Coordinates Network archives[47] for a GRB between the last ZTF nondetection (February 2.56) and the first ZTF detection (February 4.34). The only bursts consistent with the position of SN 2020bvc were detected by Konus-WIND but likely arose from an X-ray binary system that was active at the time. We conclude that SN 2020bvc had no detected GRB counterpart.

Given the lack of a detected GRB, we can use the sensitivity of the IPN spacecraft to set a limit on the isotropic-equivalent gamma-ray luminosity $L_{\gamma,\mathrm{iso}}$ of any counterpart. During the time interval of interest (16 hr), the position of SN 2020bvc was within the coded field of view of the BAT for only 5.25 hr.[48] So, we cannot set a useful limit using BAT.

Fermi/GBM had much better coverage,[49] with the position of SN 2020bvc visible most of the time (12.7 hr). Fermi/GBM is in a low-Earth (∼1.5 hr) orbit, and the position was occulted by the Earth for 10 minutes per orbit, although in six out of 10 of these occultations, the position was visible to Swift/BAT. During the interval of interest, Fermi went through five South Atlantic Anomaly passages ranging from 10 to 30 minutes in duration. Since SN 2020bvc was visible to the GBM most of the time, it is worthwhile to use the GBM sensitivity to place a limit on an accompanying GRB. For a long and soft template,[50] the GBM sensitivity is a few × 10^{-8} erg s^{-1} cm^{-2} (see the discussion in Section 2.7 of Ho et al. 2019a), so the isotropic-equivalent luminosity $L_{\gamma,\mathrm{iso}} \lesssim$ few × 10^{46} erg s^{-1}.

We obtain our most conservative lower limit on the accompanying GRB emission using Konus-WIND, which had continuous visibility of the SN 2020bvc position due to its position beyond low-Earth orbit. Assuming a Band spectral model with $\alpha = -1$, $\beta = -2.5$, and $E_{\mathrm{pk}} = 50$–500 keV, the limiting 20–1500 keV peak energy flux for a 2.944 s timescale is 1–2 × 10^{47} erg s^{-1}, corresponding to an upper limit on the peak isotropic-equivalent gamma-ray luminosity of 1.7–3.4 × 10^{47} erg s^{-1}.

For reference, classical GRBs have $L_{\gamma,\mathrm{iso}} > 10^{49.5}$ erg s^{-1} (Cano et al. 2017), and LLGRBs have $L_{\gamma,\mathrm{iso}} < 10^{48.5}$ erg s^{-1}; LLGRB 060218 had $L_{\gamma,\mathrm{iso}} = 2.6 \times 10^{46}$ erg s^{-1} (Cano et al. 2017). However, the GBM would be unlikely to detect a GRB like LLGRB 060218 accompanying SN 2006aj because of the low peak energy $E_{\mathrm{pk}} \sim 5$ keV and long duration $T_{90} \sim 2100$ s (Cano et al. 2017). Weak signals longer than 100 s look like background evolution to the GBM because the detector background can change significantly over 100–200 s. Therefore, although a classical GRB is clearly ruled out (by the lack of both a GRB and strong afterglow emission), we cannot rule out the possibility that SN 2020bvc had prompt emission identical to an LLGRB like 060218. We revisit the difficulty of ruling out an LLGRB in Section 8.

3. Light-curve Analysis

3.1. Comparisons to Other Ic-BL SNe

The P48 light curve of SN 2020bvc is shown in Figure 2, aligned with the light curve of SN 2006aj. The relative time of LLGRB 060218 is close to the time of the ATLAS nondetection, supporting our choice of the ATLAS nondetection as the

---

[47] https://gcn.gsfc.nasa.gov/gcn3_archive.html
[48] Search conducted using https://github.com/lanl/swiftbat_python.
[49] Search conducted using https://github.com/annayqho/HE_Burst_Search.
[50] A smoothly broken power law with low-energy index -1.9 and high-energy index -2.7 and $E_{\mathrm{pk}} = 70$ keV.

estimated epoch of first light, t_0. In both SN 2006aj and SN 2020bvc, the first peak fades on a timescale of 1 day, followed by the rise of the main peak of the light curve. In Section 5.2 we model the first peak as arising from shock cooling of extended low-mass material and discuss the implication of the fact that SN 2006aj and SN 2020bvc have similar first peaks.

The second peak has a rise time from first light of 13–15 days in the r band ($M_{r,\mathrm{pk}} = -18.7$ mag) and 10–12 days in the g band ($M_{g,\mathrm{pk}} = -18.3$ mag). In Figure 7, we compare the light curve to several LLGRB SNe. The timescale of the second peak is most similar to that of SN 1998bw in the r band and SN 2006aj and SN 2017iuk in the g band. The peak luminosity is intermediate to SN 2006aj and SN 1998bw. We discuss the implications in Section 5.1, where we use the light curve of the main peak to measure the properties of the explosion, such as the nickel mass, ejecta mass, and kinetic energy.

3.2. Blackbody Fits

We fit blackbody functions to the photometry of SN 2020bvc in order to measure the evolution of the bolometric luminosity L_{bol}, photospheric radius R_{ph}, and effective temperature T_{eff}. First, we manually selected 23 time bins as close as possible to epochs with observations in multiple filters. We binned the P48 light curve such that observations in a single band clustered within a few hours were averaged together. For each time bin, we constructed an SED by linearly interpolating the UV and optical light curves. The resulting SEDs are shown in Figure 8. For each SED, we used the nonlinear least-squares routine of curve_fit in scipy (Virtanen et al. 2020) to fit a blackbody. After $\Delta t = 2$ days, we excluded the UVW2 point in the fits, because it shows an excess compared to the blackbody function. To estimate the uncertainties, we performed a Monte Carlo simulation with 600 realizations of the data. The size of the error bar on each point is a 30% fractional systematic uncertainty, chosen to obtain a combined $\chi^2/\mathrm{dof} \approx 1$ across all epochs.

The fits are shown in Figure 8. The best-fit parameters are listed in Table 3 and plotted in Figure 9. Here L_{bol} peaks after $\Delta t \approx 12$–14 days at $L_{\mathrm{bol,pk}} = 4 \times 10^{42}$ erg s^{-1}, and R_{ph} increases by $v_{\mathrm{ph}} \approx 0.06c$, which is consistent with the 18,000 km s^{-1} that we measure from the spectra in Section 4.2. Using trapezoidal integration, we find a total radiated energy $E_{\mathrm{rad}} = 7.1 \times 10^{48}$ erg.

In the first panel of Figure 9, we show the evolution of L_{bol} compared to nearby LLGRB SNe. To make the comparison, we chose bolometric light curves constructed using similar filters: UBVRI for the second peak of SN 2006aj and SN 1998bw and BVRI for SN 2010bh (Cano 2013). We could not find a similar bolometric light curve for the second peak of SN 2017iuk, so we used L_{bol} from the spectral modeling of Izzo et al. (2019) and caution that this is not a direct comparison. For SN 2006aj, we also included an early measurement of the bolometric luminosity from the UVOT data (Campana et al. 2006). Objects SN 2006aj and SN 2017iuk have a similarly fast-declining first peak to SN 2020bvc; early detailed UV observations were not obtained for SN 1998bw and SN 2010bh. Overall, SN 1998bw is the most luminous LLGRB SN, followed by SN 2006aj and SN 2020bvc, which are similar to one another; SN 2010bh is significantly less luminous. We revisit these comparisons when we calculate the explosion parameters of SN 2020bvc in Section 5.
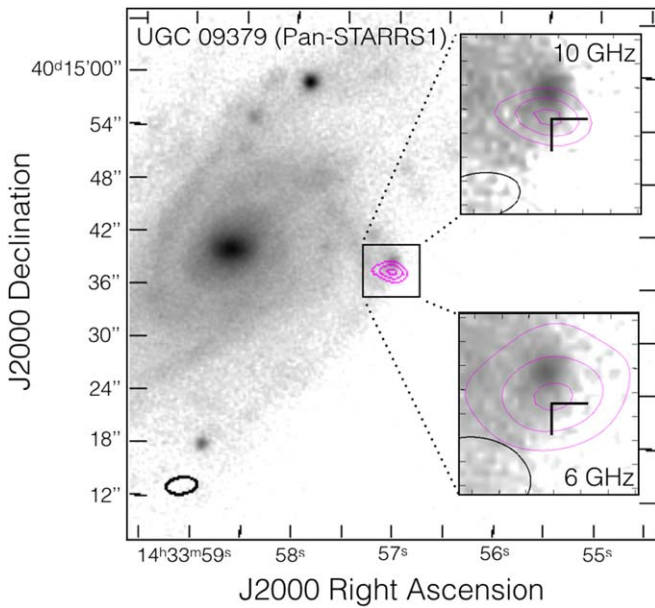
Figure 5. Image of the 10 and 6 GHz VLA observations of SN 2020bvc. The background image of UGC 09379 is from Pan-STARRS1 (Chambers et al. 2016; Flewelling et al. 2016). The radio data are overlaid as contours, and the size of the synthesized beam is shown as an ellipse in the bottom left corner. The position of the optical transient is shown as crosshairs in the zoom-in panels.
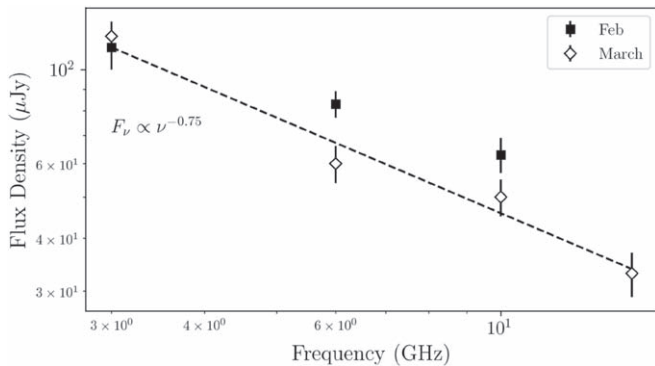

Figure 6. Radio SED of SN 2020bvc from VLA observations spanning 2 months postexplosion.

4. Spectroscopic Properties

4.1. Spectroscopic Evolution and Comparisons

As outlined in Section 2.4, we obtained 13 spectra of SN 2020bvc in the 50 days following discovery, shown in Figure 4. Here we discuss the spectroscopic evolution in more detail and compare it to LLGRB SNe.

The first spectrum ($\Delta t = 0.7$ days) is shown in the top panel of Figure 10, together with two blackbody fits. For the first fit, we allowed the temperature to vary, and found $L_{bol} = (5.62 \pm 0.25) \times 10^{42}$ erg s^{-1}, $T_{eff} = (13.21 \pm 0.27) \times 10^3$ K, and $R_{ph} = (5.09 \pm 0.10) \times 10^{14}$ cm. Here we are reporting statistical errors on the fit, but there is also considerable systematic uncertainty due to being on the Rayleigh–Jeans tail. To get a sense for what range of values is permitted, we repeated the fit fixing $T_{eff} = 20,000$ K and found $R = 3.4 \times 10^{14}$ cm and $L = 1.3 \times 10^{43}$ erg s^{-1}. In what follows, we use the parameters from the first fit.

Assuming that the value of $R_{ph} \approx 5 \times 10^{14}$ cm at $\Delta t = 0.7$ days is much larger than the value of R_{ph} at t_0, we can estimate that the mean velocity until $\Delta t = 0.7$ days is 5×10^{14} cm/0.7 days $= 0.3c$. Taking the last ZTF nondetection as t_0, the mean velocity is reduced to 5×10^{14} cm/1.8 days $= 0.1c$.

For comparison, in the top panel of Figure 10, we show a higher-resolution spectrum obtained at $\Delta t = 1.9$ days and presented in Izzo et al. (2020). We mark the Fe II and Ca II at $v_{exp} = 70,000$ km s^{-1} that Izzo et al. (2020) identified in their analysis, which are not clearly distinguishable in the SEDM spectrum. We also show early spectra of LLGRB SNe: a spectrum of LLGRB 171205A/SN 2017iuk at $\Delta t = 1.5$ hr from Izzo et al. (2019) and a spectrum of LLGRB 060218/SN 2006aj at $\Delta t = 2.6$ days from Fatkhullin et al. (2006). Both spectra are dominated by continuum, with a broad absorption feature near 5900 Å that is not clearly seen in the early spectrum of SN 2020bvc.

The next spectrum of SN 2020bvc was obtained at $\Delta t = 3.7$ days, which we show in the middle panel of Figure 10. A broad absorption feature is present at 7300 Å, which in Figure 4 appears to shift redward with time. For comparison, and to assist with identification of this feature, we compare the spectrum to two LLGRB SN spectra obtained at a similar epoch, LLGRB 060218/SN 2006aj (Fatkhullin et al. 2006) and LLGRB 171205A/SN 2017iuk (Izzo et al. 2019). The spectrum of SN 2020bvc most closely resembles that of SN 2017iuk. We show two features in the SN 2017iuk spectrum identified by Izzo et al. (2019), Ca II and Si II, at very high velocities (105,000 km s^{-1} for Ca II). Based on the similarity between the spectra, we also attribute the broad absorption feature to Ca II. To measure the expansion velocity, we measure the minimum of the absorption trough, finding $v_{exp} = 60,000$ km s^{-1} (based on the Gaussian center) and an FWHM of 0.16c, or 48,000 km s^{-1}. The spectrum of SN 2006aj shows hints of broad absorption features at similar wavelengths, but the lack of coverage on the red side makes it difficult to confirm the Ca II absorption.

After 3.7 days, the spectra of SN 2020bvc can be readily classified as Ic-BL. A spectrum of SN 2020bvc near peak optical light ($\Delta t = 13$ days) is shown in the bottom panel of Figure 10 compared to SN 2006aj and SN 2017iuk at a similar epoch. The Si II and Ca II absorption lines are clearly broader in the spectrum of SN 2020bvc than in the spectrum of SN 2006aj, although the centroids are at a similar wavelength, suggesting that the expansion velocities are similar. The absorption lines are at a higher expansion velocity in the spectrum of SN 2017iuk than in the spectrum of SN 2020bvc, although they do not appear broader.

4.2. Velocity Estimates from Fe II Features

For each spectrum after $\Delta t = 5$ days, we used publicly available code[51] from Modjaz et al. (2016) to measure the absorption (blueshift) velocities of the blended Fe II features at $\lambda\lambda 4924, 5018, 5169$, which are a proxy for photospheric velocity. The resulting velocities are listed in Table 1. Note that the fit did not converge for the NOT spectrum on March 2.14, and that we were unable to obtain satisfactory fits for the SEDM spectra.

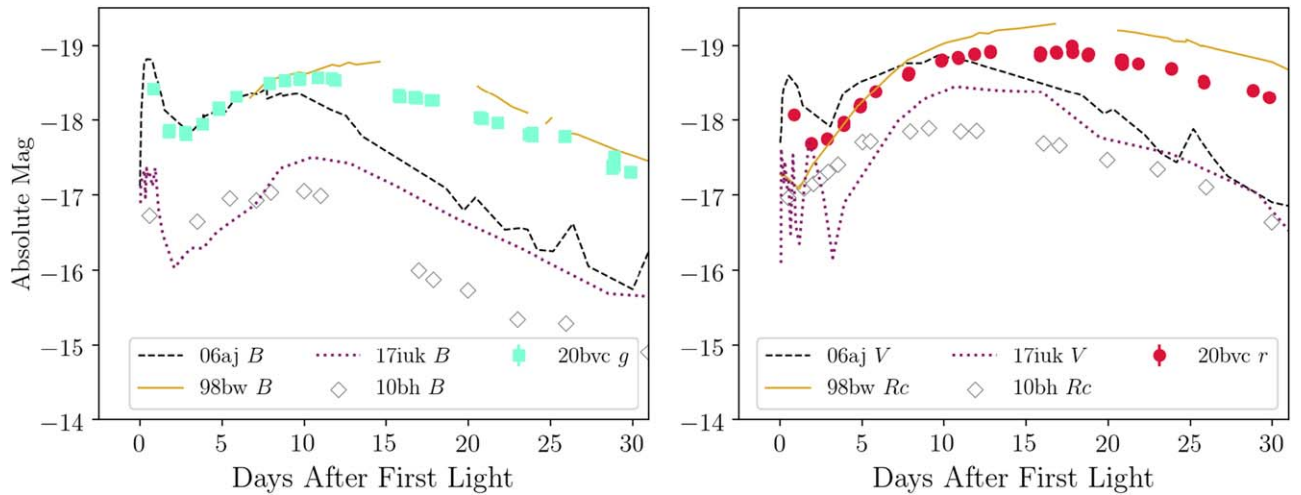In Figure 11, we compare the velocity evolution of SN 2020bvc to that of nearby LLGRB SNe. Only SN 2017iuk

---

[51] https://github.com/nyusngroup/SESNspectraLib

Figure 7. Comparison of the light curve of SN 2020bvc to nearby LLGRB SNe, shifted to a common redshift. The SN 1998bw light curve was taken from Table 2 of Clocchiatti et al. (2011), which uses data from Galama et al. (1998) and Sollerman et al. (2002), and corrected for Milky Way extinction. The SN 2006aj light curve was taken from the open SN catalog and then corrected for Milky Way extinction, with original data from Modjaz et al. (2006), Bianco et al. (2014), and Brown et al. (2014). The SN 2010bh data were taken as-is from Cano et al. (2011). The SN 2017iuk data were taken from D'Elia et al. (2018) and then corrected for Milky Way extinction.

and SN 2020bvc have spectral velocity estimates at early times, and both exhibit a steep drop during the transition from the first to the second optical peak. During the second peak, the velocities of all but SN 2010bh are similar to the velocities of Ic-BL SNe associated with GRBs, which are systematically higher than the velocities of Ic-BL SNe lacking associated GRBs (Modjaz et al. 2016).

5. Modeling the Light Curve

Double-peaked optical light curves have been observed in all types of stripped-envelope SNe: Ic-BL (with SN 2006aj as the prime example), Type Ic (Taddia et al. 2016; De et al. 2018), Type Ib (Chevalier & Fransson 2008; Mazzali et al. 2008; Modjaz et al. 2009), and Type IIb (Arcavi et al. 2011; Bersten et al. 2012, 2018; Fremling et al. 2020). The leading explanation for double-peaked light curves in these systems is that the progenitor has a nonstandard structure, with a compact core of mass M_c and low-mass material with $M_e \ll M_c$ extending out to a large radius R_e (Bersten et al. 2012; Nakar & Piro 2014; Piro 2015), although Sapir & Waxman (2017) have argued that a nonstandard envelope structure is not required.

After core collapse, a shock wave runs through the thin outer layer, and in its wake, the layer cools (the "postshock cooling" or "cooling envelope" phase), producing a short-duration first peak. The remnant is heated from within by the radioactive decay of ^{56}Ni to ^{56}Co, which dominates the light curve after a few days, producing the second peak.

In Type IIb SNe, the extended material is thought to be the stellar envelope. By contrast, Ic-BL SNe such as SN 2006aj and SN 2020bvc are thought to arise from compact stars, so the envelope is more likely to be extended material that was ejected in a mass-loss episode (Smith 2014). It is unknown why Ic-BL progenitors would undergo late-stage eruptive mass loss; possibilities include binary interaction (Chevalier 2012) and gravity waves excited by late-stage convection in the core (Quataert & Shiode 2012).

Motivated by the similarity between SN 2006aj and SN 2020bvc, we assume that the light curve of SN 2020bvc is also powered by these two components, and we calculate the properties of the explosion and the extended material.

5.1. Nickel Decay

We use the luminosity and width of the second peak of the SN 2020bvc light curve to estimate the nickel mass M_{Ni} and ejecta mass M_{ej} by fitting an Arnett model (Arnett 1982). Building on the Arnett model, Valenti et al. (2008) gave an analytic formula for $L_{bol}(t)$ as a function of M_{Ni} and a width parameter τ_m, which assumes complete trapping of gamma-rays (not significant in the regime we deal with here). Fitting the Valenti et al. (2008) light curve to the bolometric light curve from Section 3.1, we obtain $M_{Ni} = 0.13 \pm 0.01$ solar masses and $\tau_m = 8.9 \pm 0.4$ days. The fit is shown in Figure 12.

The value of M_{Ni} we obtain for SN 2020bvc is similar to the literature estimates for SN 2006aj ($M_{Ni} = 0.20 \pm 0.10\,M_\odot$; Cano et al. 2017) and smaller than the nickel mass of SN 1998bw (0.3–0.6 $M_\odot$; Cano et al. 2017), which is consistent with the relative luminosity of the bolometric light curves (Figure 9).

Next, we solve for M_{ej} and the explosion energy E_k using Equations (2) and (3) in Lyman et al. (2016). Taking the opacity $\kappa = 0.1\ \mathrm{cm^2\,g^{-1}}$ (close to the value found from spectral modeling of Ic-BL SNe near peak; Mazzali et al. 2000) and $v_{ph} = 18{,}000\ \mathrm{km\,s^{-1}}$ (Section 4.2), we find $M_{ej} = 2.2 \pm 0.4\,M_\odot$, where the uncertainty is dominated by the 20% uncertainty on v_{ph}. The resulting kinetic energy is $E_K = 0.5\,M_{ej}\,v_{ph}^2 = 7.1 \pm 2.8 \times 10^{51}$ erg. The explosion parameters for SN 2020bvc are summarized in Table 4.

5.2. Shock Cooling

The mass M_e and radius R_e of the material surrounding the progenitor can be estimated using the timescale and luminosity of the first peak. In Section 4.1 we measured a lower limit on the peak bolometric luminosity $L_{bol} > 5.62 \times 10^{42}$ erg s^{-1}, with an upper limit on the time to peak of 0.7 days. From our calculation in Appendix B, we obtain an upper limit on $M_e < 10^{-2}\,M_\odot$ and a
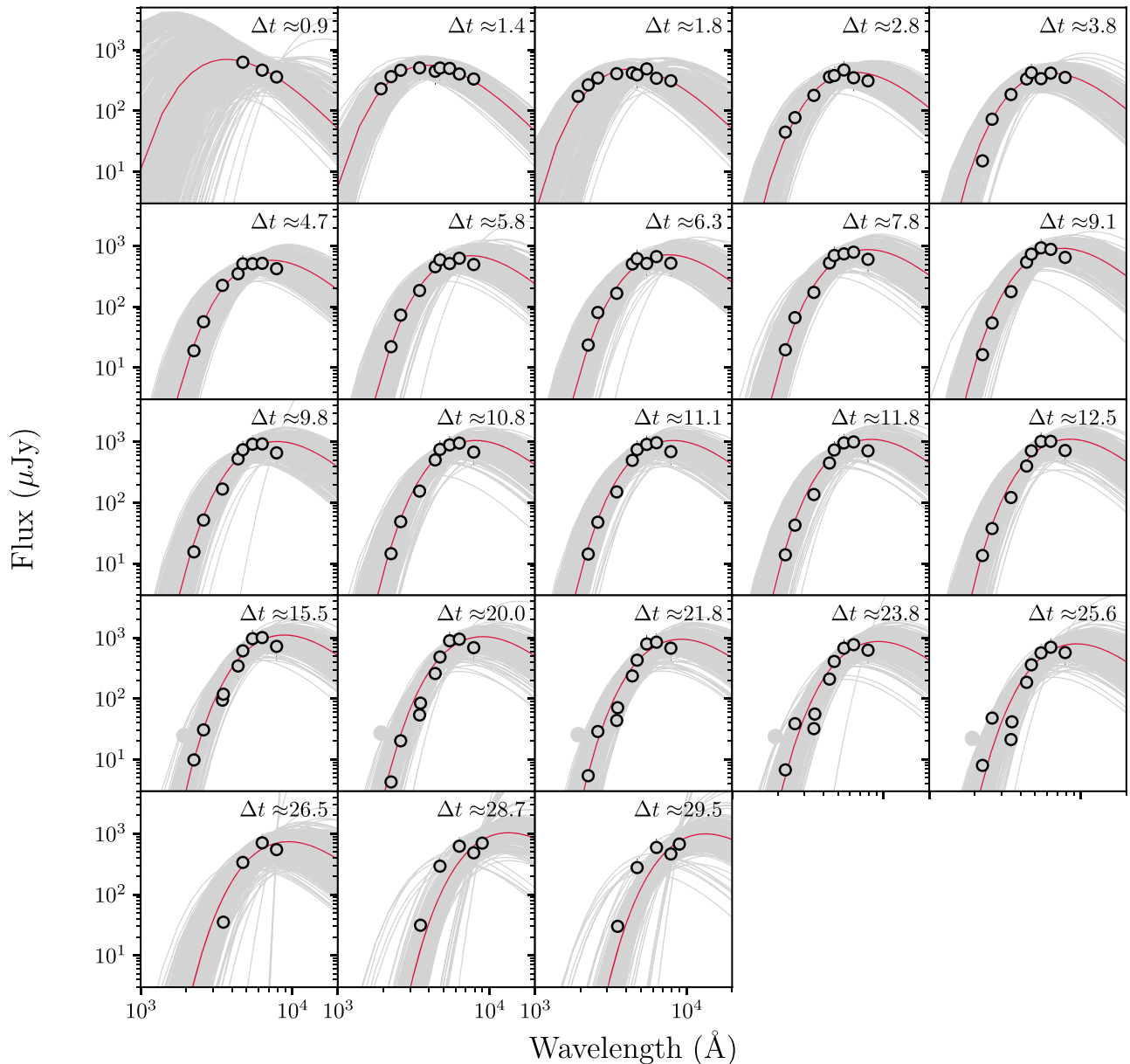
Figure 8. Blackbody fits to optical and Swift/UVOT photometry of SN 2020bvc. The photometry has been interpolated onto common epochs as described in Section 3.2. The fit was run through a Monte Carlo with 600 realizations of the data. Individual fits are shown as thin gray lines; the dispersion corresponds to the overall uncertainties in the fits. Only outlined points were included in the fits.

lower limit on $R_e > 10^{12}$ cm. In Figure 12, we show that the bolometric light curve is well described by the sum of the shock-cooling model from Appendix B with $R_e = 4 \times 10^{12}$ cm and $M_e = 10^{-2}\,M_\odot$ and an ^{56}Ni-powered light curve with the properties calculated in Section 5.1. The shock-cooling light curve only describes the decline after peak; we do not attempt to model the rise. The properties of the ambient material are summarized in Table 4.

The values of M_e and R_e we measured for SN 2020bvc are consistent with what was inferred for SN 2006aj, which had much more detailed early UV and optical data: $M_e = 4 \times 10^{-3}\,M_\odot$ and $R_e = 9 \times 10^{12}$ cm (Irwin & Chevalier 2016). A similar low-mass shell was inferred for the Ic-BL SN 2018gep (Ho et al. 2019a); in that case, the shell ($M_e = 0.02\,M_\odot$) was at a larger radius ($R_e = 3 \times 10^{14}$ cm), which prolonged the shock-interaction peak and blended it with the ^{56}Ni-powered peak. A similarly low-mass, large-radius shell may also explain the luminous light

curve of the Ic-BL SN iPTF16asu (Whitesides et al. 2017). With these four events, we may be seeing a continuum in shell properties around Ic-BL SNe resulting from different mass-loss behavior just prior to core collapse (Smith 2014).

6. Modeling the Fast Ejecta

One of the key features of LLGRB 060218/SN 2006aj was radio and X-ray emission that peaked earlier and was more luminous than that of ordinary CC SNe. Here we compare the early (1–50 days) radio and X-ray properties of SN 2020bvc to those of SN 2006aj and other LLGRB SNe.

6.1. Radio Emission

We have several reasons to believe that the radio emission is dominated by the transient rather than the host galaxy. First, the flux density is observed to decline at 6 and 10 GHz, albeit

Table 3
Blackbody Evolution of SN 2020bvc

Δt (days)	L_{bol} (10^{42} erg s^{-1})	T_{eff} (10^3 K)	R_{ph} (10^{14} cm)
0.67	5.6 ± 0.3	13.2 ± 0.3	5.1 ± 0.1
0.9	$5.4^{+6.2}_{-2.7}$	$13.3^{+4.6}_{-3.8}$	$5.0^{+2.0}_{-1.2}$
1.4	$3.8^{+0.7}_{-0.4}$	$12.2^{+1.2}_{-1.2}$	$4.9^{+0.9}_{-0.7}$
1.8	$3.1^{+0.5}_{-0.9}$	$11.3^{+1.4}_{-2.3}$	$5.1^{+2.1}_{-0.9}$
2.8	$1.8^{+0.2}_{-0.3}$	$7.6^{+1.0}_{-1.2}$	$8.9^{+2.9}_{-1.9}$
3.8	$1.8^{+0.2}_{-0.2}$	$7.4^{+0.9}_{-0.6}$	$9.1^{+1.8}_{-1.7}$
4.7	$2.1^{+0.3}_{-0.2}$	$6.8^{+1.3}_{-0.9}$	$11.7^{+4.6}_{-3.5}$
5.8	$2.4^{+0.3}_{-0.3}$	$6.6^{+1.1}_{-1.0}$	$13.6^{+5.8}_{-3.8}$
6.3	$2.5^{+0.3}_{-0.3}$	$6.5^{+1.1}_{-1.1}$	$14.5^{+6.6}_{-4.2}$
7.8	$3.0^{+0.4}_{-0.4}$	$6.3^{+0.7}_{-1.0}$	$16.3^{+7.1}_{-3.0}$
9.1	$3.3^{+0.4}_{-0.5}$	$6.4^{+0.7}_{-0.5}$	$16.6^{+3.8}_{-3.9}$
9.8	$3.4^{+0.4}_{-0.4}$	$6.1^{+0.6}_{-0.9}$	$18.7^{+6.5}_{-3.6}$
10.8	$3.4^{+0.4}_{-0.4}$	$5.9^{+0.6}_{-0.9}$	$19.9^{+6.5}_{-3.9}$
11.1	$3.5^{+0.4}_{-0.4}$	$5.9^{+0.8}_{-0.8}$	$20.5^{+6.1}_{-4.7}$
11.8	$3.5^{+0.4}_{-0.5}$	$5.7^{+0.7}_{-0.7}$	$21.6^{+5.4}_{-4.5}$
12.5	$3.6^{+0.4}_{-0.6}$	$5.6^{+0.6}_{-0.6}$	$22.2^{+5.3}_{-3.7}$
15.5	$3.4^{+0.5}_{-0.5}$	$5.4^{+0.6}_{-0.5}$	$23.2^{+5.0}_{-4.6}$
20.0	$3.1^{+0.4}_{-0.5}$	$5.3^{+0.4}_{-0.4}$	$23.3^{+4.6}_{-4.1}$
21.8	$2.8^{+0.4}_{-0.5}$	$5.2^{+0.4}_{-0.3}$	$23.5^{+3.7}_{-4.3}$
23.8	$2.6^{+0.4}_{-0.5}$	$5.2^{+0.5}_{-0.3}$	$22.4^{+3.8}_{-4.4}$
25.6	$2.3^{+0.3}_{-0.4}$	$5.1^{+0.4}_{-0.3}$	$21.6^{+3.6}_{-3.9}$
26.5	$2.2^{+0.4}_{-0.4}$	$5.1^{+0.6}_{-0.3}$	$21.2^{+4.6}_{-5.0}$
28.7	$2.1^{+0.3}_{-0.3}$	$3.6^{+0.2}_{-0.2}$	$40.7^{+7.3}_{-4.1}$
29.5	$2.0^{+0.4}_{-0.3}$	$3.6^{+0.2}_{-0.2}$	$40.6^{+6.9}_{-4.9}$

Note. The first epoch is from fitting the optical spectrum (Section 4). The remaining epochs are from fitting multiband photometry (Section 3.2).

marginally. Second, in Section 2.6 we found that the source is unresolved (i.e., a point source) at all frequencies. Third, at all frequencies, the centroid of the radio source is consistent with the position of the optical transient, and there is no other radio source detected in the vicinity of the galaxy. (There is a nearby H II region, but this would produce free–free emission and therefore a flat spectral index, which is inconsistent with our observations.) Late-time radio observations will be used to be secure and to subtract any host contribution.

If the emission at 3 GHz is entirely from the underlying host-galaxy region (the synthesized beamwidth at this frequency is 7″), the flux density at this frequency can be used to estimate a star formation rate of $0.2\,M_\odot$ yr^{-1} using the prescription (Murphy et al. 2011; Greiner et al. 2016)

$$\left(\frac{\text{SFR}_{\text{Radio}}}{M_\odot\ \text{yr}^{-1}}\right) = 0.059\left(\frac{F_\nu}{\mu\text{Jy}}\right)(1+z)^{-(\alpha+1)}$$
$$\times \left(\frac{D_L}{\text{Gpc}}\right)^2\left(\frac{\nu}{\text{GHz}}\right)^{-\alpha}, \qquad (1)$$

where we use $F_\nu = 120\,\mu$Jy, $\nu = 3$ GHz, and $\alpha = -0.9$ for $F_\nu \propto \nu^\alpha$.

For now, we assume that the radio emission is primarily from the transient. In Figure 13, we show the 10 GHz radio light curve of SN 2020bvc. The luminosity is similar to that of SN 2006aj and SN 2010bh and significantly fainter than that of SN 2017iuk and SN 1998bw. In Ho et al. (2019b), we found that the peak radio luminosity is directly proportional to U/R, the (thermalized)
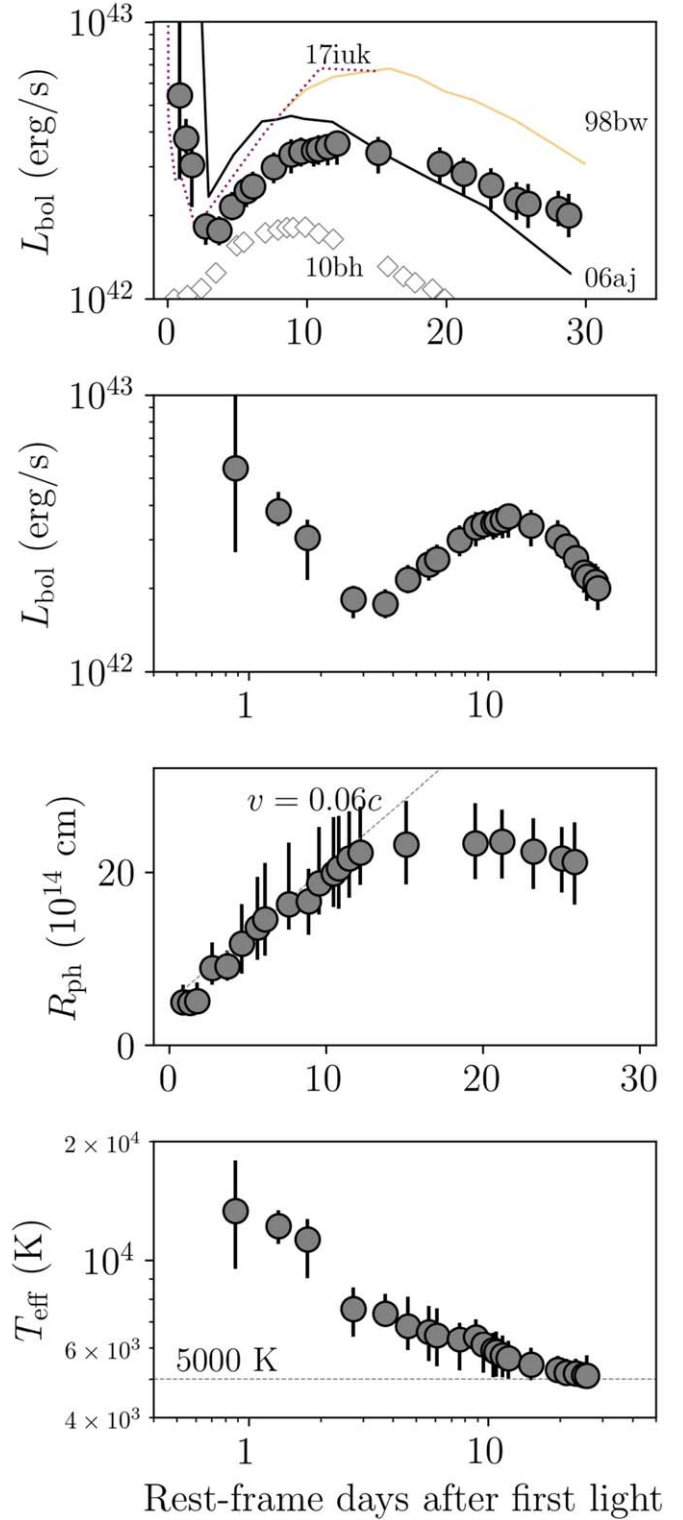

Figure 9. Blackbody evolution of SN 2020bvc. First panel: bolometric light curve compared to LLGRB SNe: SN 2006aj and SN 1998bw (*UBVRI*; Cano 2013), SN 2010bh (*BVRI*; Cano 2013), and SN 2017iuk (spectral modeling; Izzo et al. 2019). We add early L_{bol} measurements of SN 2006aj from Campana et al. (2006). Second panel: bolometric light curve in log–log space. Third panel: photospheric radius, with a dotted line indicating $v = 18,000$ km s^{-1}. Fourth panel: effective temperature, with a horizontal line marking 5000 K, the recombination temperature of carbon and oxygen.

energy of the blast wave divided by the shock radius. So, the lower radio luminosity of SN 2006aj and SN 2020bvc could correspond to a lower explosion energy. This is consistent with the finding in
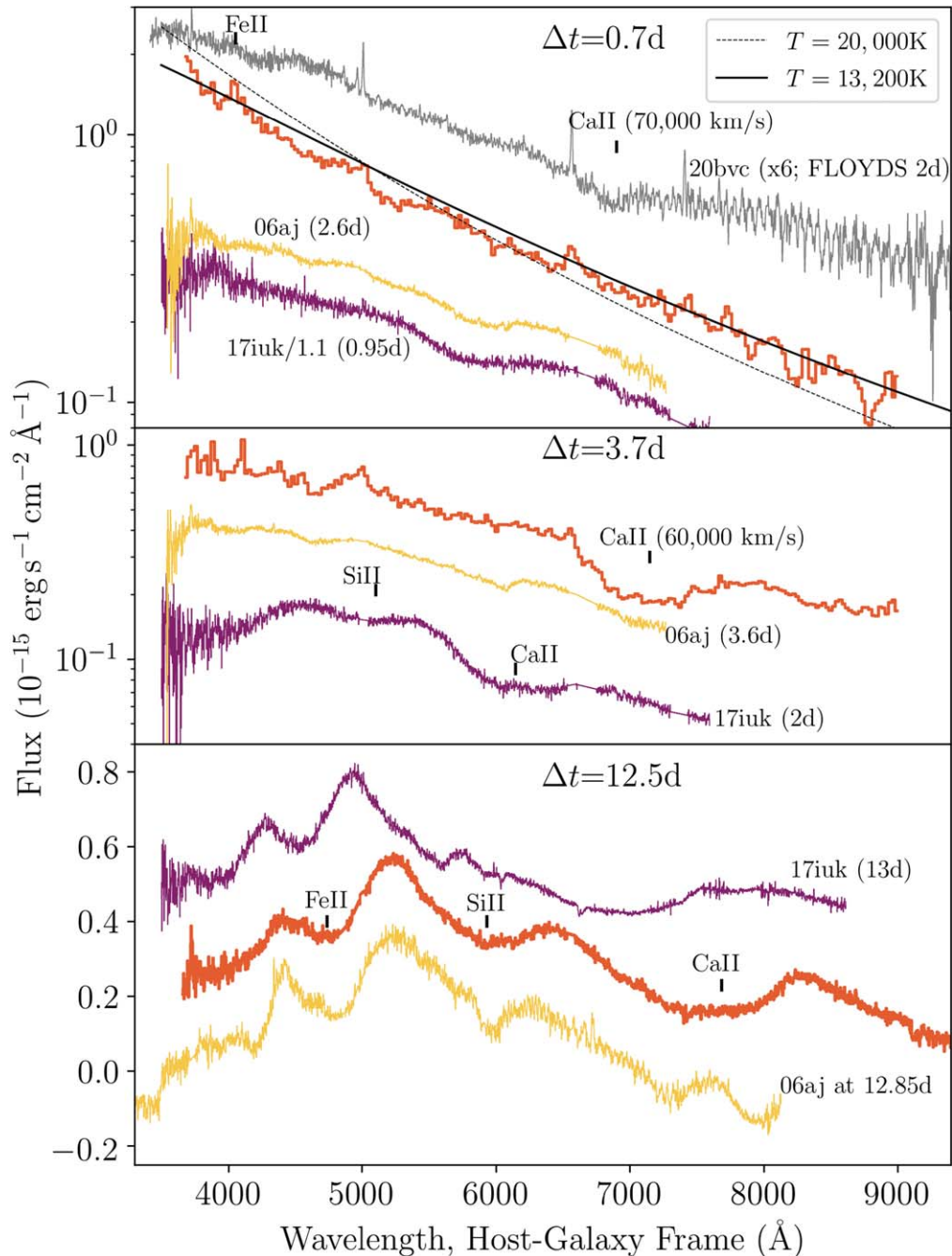
Figure 10. Spectra of SN 2020bvc compared to spectra of LLGRB 171205A/SN 2017iuk (from Izzo et al. 2019) and LLGRB 060218/SN 2006aj (from Fatkhullin et al. 2006; Modjaz et al. 2006/WISeREP) at similar epochs. In the top panel, we also show the blackbody fits described in Section 4 and the spectrum of SN 2020bvc at $\Delta t = 1.9$ days downloaded from WISeREP (Hiramatsu et al. 2020) and obtained by the FLOYDS-N instrument on the Faulkes Telescope North (Brown et al. 2013). The identification of Fe II and Ca II at 70,000 km s^{-1} is from Izzo et al. (2020).

Section 5.1 that SN 2006aj and SN 2020bvc have a similar kinetic energy, which is significantly smaller than the kinetic energy of SN 1998bw and SN 2017iuk.

From the radio SED, we estimate that the peak frequency is <3 GHz at $\Delta t = 24$ days, with a peak flux density >113 μJy. We use these values and the framework described in Chevalier (1998) to estimate properties of the forward shock and ambient medium. We list the results in Table 5, discuss the implications here, and provide the calculation in Appendix C. In Figure 14, we show the peak frequency and time compared to the peak luminosity, with lines indicating how these values correspond to ambient density (mass-loss rate) and energy.

First, we find a forward shock radius of 1.7×10^{16} cm, implying a mean velocity up to 24 days of $\Gamma\beta > 0.28$. As shown in Figure 14, the lower limit on the velocity we infer is similar to the mildly relativistic velocities inferred for some LLGRB SNe, in particular SN 2010bh. It is also possible that the velocity approaches the relativistic speeds inferred for SN 2006aj and SN 1998bw.

Second, we find a lower limit on the energy thermalized by the shock of 1.3×10^{47} erg. As shown in Figure 14, SN 2020bvc appears to have an energy most similar to that of SN 2006aj and a radio-loud Ic-BL SN recently discovered in ZTF (Ho et al. 2020b).
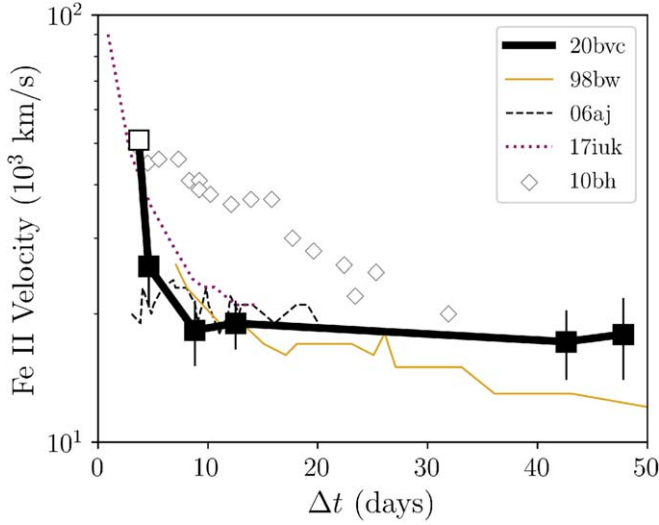
Figure 11. Velocity of SN 2020bvc (black) compared to LLGRB SNe. Open symbols correspond to Ca II velocity measured from the absorption-line minimum, and filled symbols correspond to velocities measured by fitting the Fe II absorption complex. Velocities come from Izzo et al. (2019) for SN 2017iuk and Modjaz et al. (2016) for all other SNe. Modjaz et al. (2016) reported velocities from the peak of the optical light curve, so we shifted to time since GRB using Galama et al. (1998) for SN 1998bw, Campana et al. (2006) for SN 2006aj, and Bufano et al. (2012) for SN 2010bh.
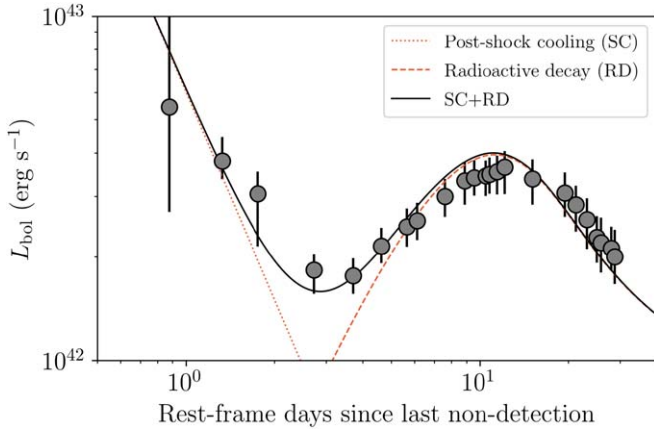
Figure 12. Bolometric luminosity evolution of SN 2020bvc. The shock-cooling model from Section 5.2 is shown as a dotted orange line. The radioactive decay model from Section 5.1 is shown as a dashed line. The black line is the sum of the two models.

Table 4
Explosion Properties of SN 2020bvc

Parameter	Value
E_k (10^{51} erg)	7.1 ± 2.8
$M_{\rm ej}$ ($M_\odot$)	2.2 ± 0.4
$M_{\rm Ni}$ ($M_\odot$)	0.13 ± 0.01
M_e ($M_\odot$)	<0.01
R_e (cm)	$>10^{12}$

Third, we find an ambient density of $n_e = 160$ cm^{-3}, which we show in Figure 14 as a mass-loss rate of $\sim 10^{-5}\,M_\odot$ yr^{-1}, assuming a wind velocity $v_w = 1000$ km s^{-1}. As shown in the figure, this mass-loss rate is within an order of magnitude of LLGRB SNe, including SN 2006aj, SN 1998bw, and SN 2010bh.
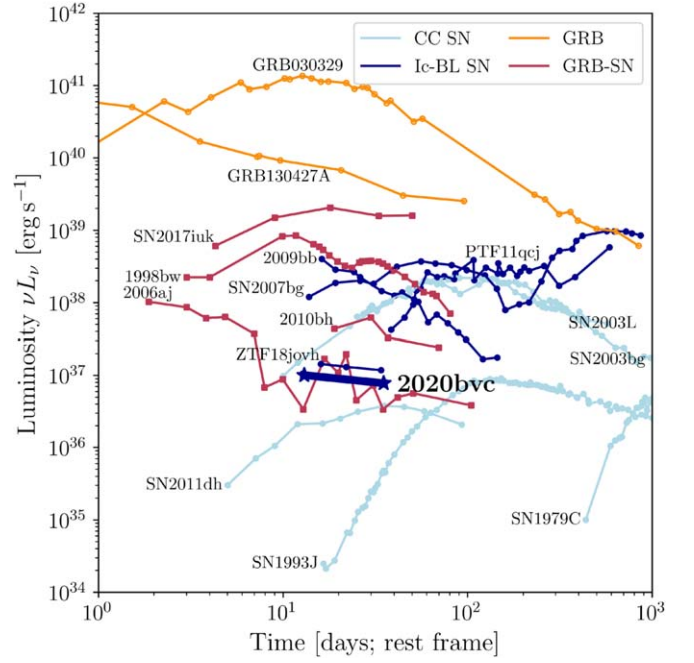
Figure 13. The 10 GHz radio light curve of SN 2020bvc (points) compared to LLGRBs and relativistic Ic-BL SNe. The light curve of GRB 130427A is the 6.8 GHz light curve from Perley et al. (2014). The data point for SN 2017iuk is at 6 GHz (Laskar et al. 2017). The SN 2006aj data are at 8.5 GHz from Soderberg et al. (2006). The ZTF 18aaqjovh data are from ?. The SN 2010bh light curve is at 5.4 GHz from Margutti et al. (2014). The PTF 11qcj light curve is at 5 GHz from ?. All other sources are as described in Appendix C of Ho et al. (2019b).

Table 5
Properties of the Forward Shock in SN 2020bvc Derived from Radio and X-Ray Observations at $\Delta t = 24$ days

Parameter	Value
$\nu_a = \nu_p$ (GHz)	<3
$F_{\nu,p}$ (μJy)	>110
R (cm)	$>1.7 \times 10^{16}$
v/c	>0.3
B (G)	<0.34
U (erg)	1.5×10^{47}
n_e (cm^{-3})	160
ν_c (Hz)	1.4×10^{13}

Fourth, we find that the cooling frequency is $\nu_c = 1.0 \times 10^{13}$ Hz, below the X-ray band. We discuss the implications in Section 6.2.

Finally, we address the model proposed in Izzo et al. (2020), that SN 2020bvc represents a GRB jet with energy 2×10^{51} erg viewed at an angle of 23° ($\theta_{\rm obs} = 0.4$) propagating into a power-law density profile $R^{-1.5}$. The authors argued that this event has similar early optical behavior to LLGRB 171205A/SN 2017iuk and that the X-ray emission is consistent with the predicted light curve from Granot et al. (2018). We point out that the same model predicts an 8.5 GHz radio light curve that exceeds 10^{30} erg s^{-1} Hz^{-1} over the period of our VLA observations, several orders of magnitude more luminous than our measurements. An off-axis jet cannot be entirely ruled out; future radio observations will be needed to determine whether a highly off-axis jet could be present. However, for now, we find that no off-axis jet is required to explain the 1–50 day radio
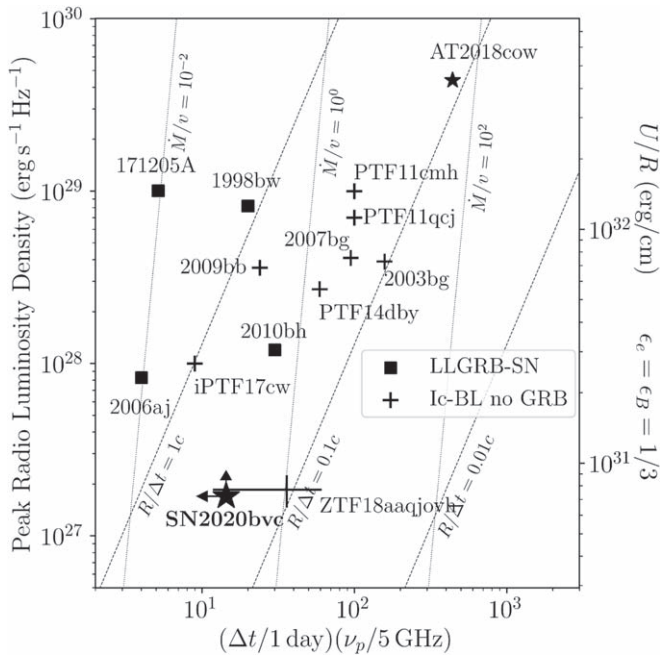
Figure 14. Luminosity and peak frequency of the radio light curve of SN 2020bvc compared to LLGRBs and energetic SNe. Lines of constant mass-loss rate (scaled to wind velocity) are shown in units of $10^{-4}\,M_\odot\,\mathrm{yr}^{-1}/$ 1000 km s^{-1}. Data for PTF 14dby are from the 7.4 GHz light curve in Corsi et al. (2016). Data for PTF 11cmh and PTF 11qcj are from the 5 GHz light curve in Corsi et al. (2016). Data for iPTF 17cw are from the 2.8 GHz light curve in Corsi et al. (2017). Data for ZTF 18aaqjovh are from Ho et al. (2020b). For details on all other sources, see caption to Figure 5 and Appendix C in Ho et al. (2019b).

light curve (a similar argument was made for SN 2006aj; Soderberg et al. 2006). To our knowledge, only one radio data point has been published for SN 2017iuk, and the radio emission compared to off-axis models was not discussed in Izzo et al. (2019).

In conclusion, the radio properties of SN 2020bvc are similar to what has been observed for LLGRB SNe. Although we do not have evidence for relativistic ejecta or a GRB, the radio light curve is unlike what has been seen for "ordinary" core-collapse SNe, suggesting that SN 2020bvc is related to the LLGRB phenomenon, i.e., an LLGRB-like event discovered optically.

6.2. X-Ray Emission

In this section, we compare the X-ray light curve and X-ray–to–radio SED of SN 2020bvc to those of SN 2006aj and other LLGRBs in the literature.

The X-ray light curve of LLGRB 060218/SN 2006aj had two components: the prompt emission itself, which lasted until 10^4 s (often called a GRB, but given the low peak energy, it is also called an X-ray flash), and an afterglow that decayed as $t^{-\alpha}$, where $\alpha = 1.2 \pm 0.1$ until 10^6 s (Campana et al. 2006; Soderberg et al. 2006). The 0.3–10 keV luminosity was 8×10^{41} erg s^{-1} at 3 days postexplosion (Campana et al. 2006). In Figure 15, we show the 0.3–10 keV light curve of SN 2020bvc compared to that of SN 2006aj and nearby LLGRB SNe. We find that the X-ray luminosity is within an order of magnitude of SN 2006aj, as well as SN 1998bw and SN 2010bh.

Next, we consider the radio–to–X-ray spectral index. At $\Delta t = 13$ days, the radio–to–X-ray spectral index of SN 2020bvc is $\beta_{RX} = 0.5$, where $F_\nu \propto \nu^{-\beta}$. Given that the cooling frequency
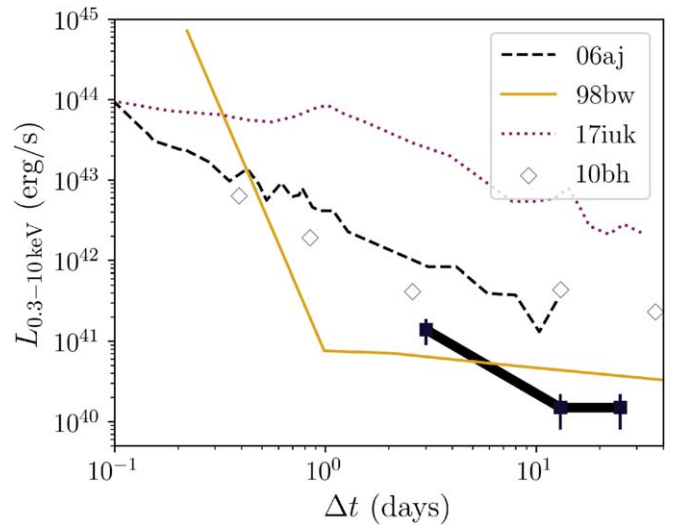
Figure 15. The 0.3–10 keV X-ray light curve of SN 2020bvc (black connected squares) compared to that of nearby Ic-BL SNe associated with LLGRBs. Data on GRB SNe are taken from Campana et al. (2006), Corsi et al. (2017), and D'Elia et al. (2018).
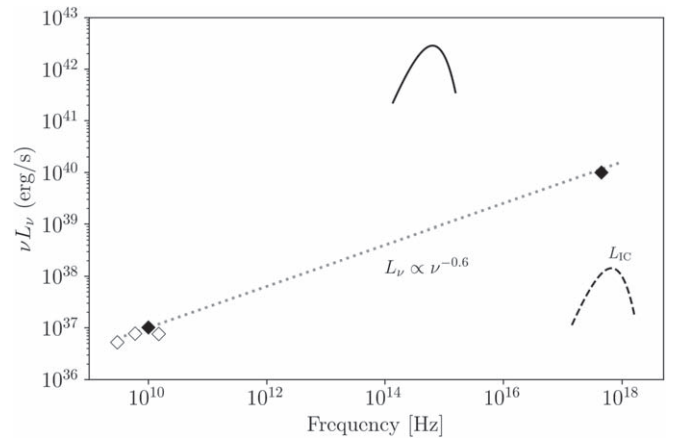
Figure 16. SED from radio to X-rays at $\Delta t = 13$ days. The open diamonds are VLA data points from 17–28 days. The solid line is the blackbody fit to the optical SED. The dotted line shows an extrapolation of $L_\nu \propto \nu^{-(p-1)/2}$, where $p = 2.2$, and the dashed curve shows the predicted emission from inverse Compton scattering (calculated in Appendix D).

lies below the X-ray band (Section 6), the value of β_{RX} is too shallow for the X-rays to be an extension of the radio synchrotron spectrum. The same was true of SN 2006aj, which had a very similar value of $\beta_{RX} = 0.5$ (Fan et al. 2006; Soderberg et al. 2006; Irwin & Chevalier 2016).

Furthermore, for the X-rays to be an extension of the synchrotron spectrum, we would require $\nu_c > 10^{17}$ GHz at $t \approx 30$ days and therefore $B < 0.01$ G, which is over an order of magnitude smaller than the value of B measured in any known SN (Chevalier 1998; Chevalier & Fransson 2006; Corsi et al. 2016). This is another argument for why the X-rays are unlikely to arise from the same synchrotron spectrum as the radio emission.

Finally, from the ratio of the optical to radio luminosity, we can estimate the expected contribution of X-rays from inverse Compton scattering. We find (Appendix D) that the contribution is not sufficient to explain the X-ray luminosity that we observe, which, again, was also the case in SN 2006aj. The X-ray "excess" observed in SN 2006aj has been attributed to the long-lived activity of a central engine (Fan et al. 2006; Soderberg et al. 2006) and to
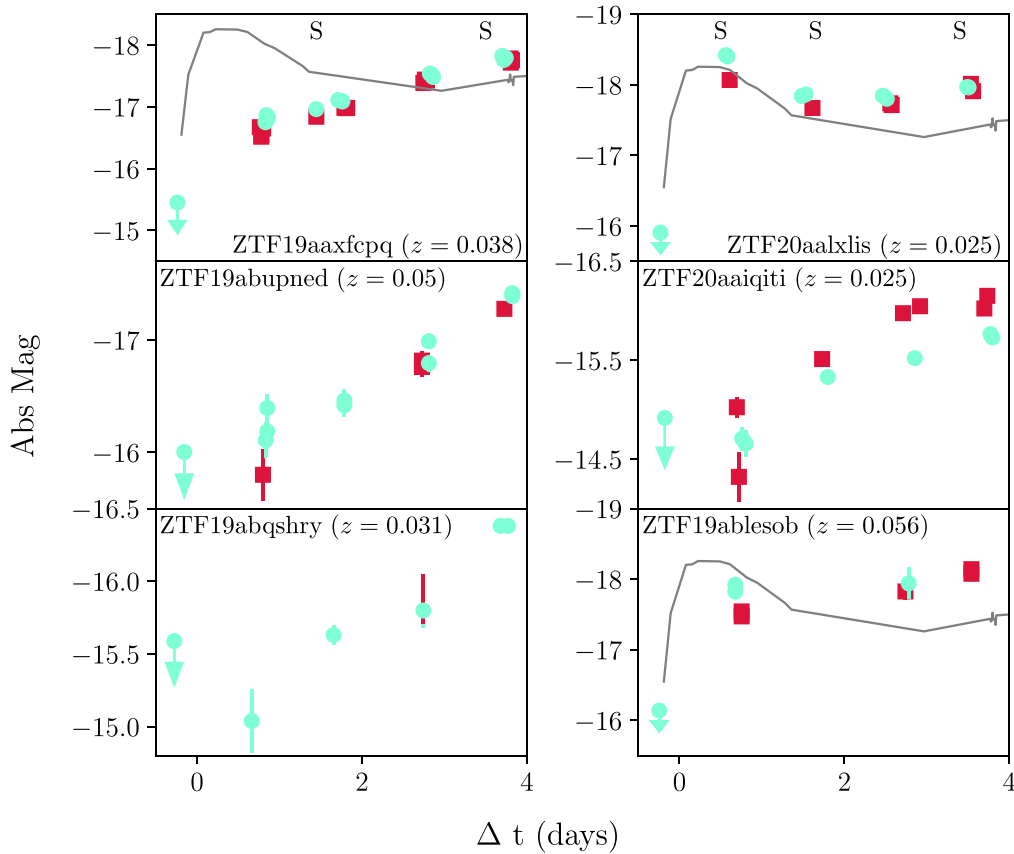
Figure 17. Early ($\Delta t \lesssim 4$ days) light curves of nearby Ic-BL SNe observed as part of ZTF's high-cadence surveys from forced photometry on P48 images (Yao et al. 2019). The B-band light curve of SN 2006aj is shown as a gray line for comparison. Epochs of follow-up spectroscopy are marked with an "S" along the top of the panel.

dust scattering (Margutti et al. 2015; Irwin & Chevalier 2016). On the other hand, Waxman et al. (2007) argued that the long-lived X-ray emission could be explained naturally in a model of mildly relativistic shock breakout into a wind, and that it was the radio emission that required a separate component. The data we have are less detailed than those obtained for SN 2006aj, so they are not useful in distinguishing between these different possibilities.

7. Early ZTF Light Curves of Nearby Ic-BL SNe

As discussed in Section 5.2, the timescale and luminosity of the shock-cooling peak are most sensitive to the shell properties (mass, radius) and shock velocity. By contrast, the timescale and luminosity of the radioactively powered peak are set by the nickel mass, ejecta mass, and explosion energy. So, it is not obvious that the properties of the second peak (which are heterogeneous; Taddia et al. 2019) should be correlated with the properties of the first peak.

In Figure 17, we show early (<4 days) light curves of five nearby ($z \lesssim 0.05$) Ic-BL SNe observed as part of ZTF's high-cadence surveys, which were spectroscopically classified as part of the ZTF flux-limited (Fremling et al. 2020) and volume-limited (De et al. 2019) experiments. The light curves shown are from forced photometry on P48 images (Yao et al. 2019), and epochs of spectroscopy are marked with an "S." For the two most luminous events, we show the light curve of SN 2006aj for comparison. We can rule out a first peak like that of SN 2006aj (duration ≈ 1 days, peak luminosity ≈ -18) for all events except one (ZTF 19ablesob). Note that the faintest LLGRB SN, SN 2010bh, peaked at $M = -17$ mag; with the ZTF flux-limited survey, we would be

over 90% complete for such events out to $z = 0.03$. SN 2020bvc peaked brighter than $M = -18.5$, so the flux-limited survey would be over 90% complete for such events out to $z = 0.06$.

Our high-cadence optical observations provide the first evidence that Ic-BL SNe like LLGRB 060218/SN 2006aj are not the norm. Radio follow-up observations have only been sensitive enough to show that events like LLGRB 980425/SN 1998bw are uncommon (Corsi et al. 2016) and in most cases have been unable to rule out emission like that seen in SN 2006aj and SN 2020bvc.

There are many degeneracies that complicate the interpretation of Figure 17. Rise time and peak luminosity are sensitive to the velocity of the shock. The shock velocity when it breaks out of the star is sensitive to the outer density gradient in the stellar envelope and the energy of the explosion. Even if all Ic-BL progenitors were identical, there could be a strong dependence with observing angle. Ic-BL SNe are expected to be asymmetric and bipolar, so the ejecta directed along the poles will move faster than along the equator. Thus, an event viewed along the poles could have a much brighter shock-interaction peak.

Finally, assuming identical and spherically symmetric explosions for the Ic-BL SNe, there could be wide diversity in the properties of the ambient material, i.e., mass, radius, and geometry. The circumstellar medium (CSM) itself could be asymmetric (e.g., a disk rather than a spherical wind), introducing even more complicated viewing-angle effects.

As we discussed in our analysis of another fast-rising luminous Ic-BL SN, SN 2018gep (Ho et al. 2019a), it can be difficult to know when it is appropriate to model such emission

as arising from shock breakout in low-mass, large-radius material and when it is appropriate to model such emission as arising from postshock cooling in higher-mass, smaller-radius material (e.g., Nakar & Piro 2014; Piro 2015). In short, it is extremely difficult at present to explain why we see such diversity in the early light curves of Ic-BL SNe. A model grid of different explosion and CSM properties with the resulting light curves is in preparation (D. K. Khatami et al. 2020, in preparation) and will be useful in understanding what configurations are ruled out or allowed for each of the objects in Figure 17.

8. Summary and Discussion

We presented optical, X-ray, and radio observations of SN 2020bvc, which shares key characteristics with the Ic-BL SN 2006aj associated with LLGRB 060218. Both events had the following.

1. A double-peaked optical light curve. The first peak is fast (≈ 1 day), luminous ($M = -18$), and blue ($g-r \approx -0.3$ mag) and can be modeled as shock-cooling emission from low-mass ($M_e < 10^{-2} M_\odot$) extended ($R_e > 10^{12}$ cm) material.
2. Radio emission (10^{37} erg s^{-1} at 10 GHz) from a mildly relativistic ($v > 0.3c$) forward shock, much fainter than that observed in LLGRB SNe such as SN 1998bw and SN 2017iuk.
3. X-ray emission of a similar luminosity (10^{41} erg s^{-1}) that likely requires a separate emission component from that producing the radio emission.

When our paper was nearly complete, Izzo et al. (2020) presented an interpretation of SN 2020bvc as a classical high-energy (2×10^{51} erg) GRB viewed 23° off-axis on the basis of (1) the fast expansion velocities ($v_{exp} \approx 70,000$ km s^{-1}) measured from the early optical spectra, similar to those observed in the Ic-BL SN 2017iuk accompanying LLGRB 171205A; (2) the X-ray light curve; and (3) the double-peaked UVOT light curve, where the first peak was argued to arise from the cocoon expanding and cooling after breaking out of the progenitor star. In our work, we found that from the perspective of the radio observations obtained so far (1–50 days postdiscovery), no off-axis jet is required. In particular, the faint radio light curve is not consistent with the model in Granot et al. (2018) invoked by Izzo et al. (2020) to explain the X-ray data.

Instead, the simplest explanation from our data is that SN 2020bvc is a similar event to LLGRB 060218/SN 2006aj. The latter has been extensively modeled, and a summary of leading interpretations can be found in Irwin & Chevalier (2016). Here we outline the different models, then discuss how high-cadence optical surveys, together with early spectroscopy and X-ray and radio follow-up observations, can help distinguish between them.

1. *Mildly relativistic shock breakout into a wind.* Campana et al. (2006) and Waxman et al. (2007) proposed that this single mechanism was responsible for the LLGRB, the shock-cooling emission, and the X-ray afterglow, in which case all three would be isotropic (a different low-energy component would be needed for the radio emission).
2. *Choked jet.* Nakar (2015) expanded on the model above by suggesting that the shock breakout is powered by an

energetic GRB-like jet that is choked in extended low-mass material surrounding the progenitor star. Again, all emission components would be expected to be isotropic.
3. *On-axis low-power jet.* Irwin & Chevalier (2016) proposed that the LLGRB and the shock-cooling emission are decoupled; the LLGRB was produced by a successful collimated low-power jet and the shock-cooling emission by spherical SN ejecta. In that case, the LLGRB would only be observable within a small viewing angle, while the shock-cooling emission would be isotropic.

In Section 7 we found that a number of Ic-BL SNe lack luminous early peaks. If X-ray and radio observations of such events reveal LLGRB-like X-ray and radio emission, and shock-cooling emission is expected to be isotropic, this would argue against a single mechanism for the shock-cooling emission and the afterglow. If, on the other hand, a double-peaked optical light curve is predictive of LLGRB-like X-ray and radio emission, and single-peaked events lack such emission, that would support models in which these components are produced by the same mechanism. Another test is the relative rates: if the LLGRB is only observable within a small viewing angle, the rate of double-peaked Ic-BL SNe should significantly exceed the rate of LLGRBs.

The key argument that LLGRB 171205A/SN 2017iuk arose from a jet was the presence of iron-peak elements in the early spectra, thought to have been transported to the surface by the jet (Izzo et al. 2019). SN 2017iuk was discovered via a GRB trigger, but with SN 2020bvc, we have demonstrated that high-cadence optical surveys can enable similarly early spectroscopic observations. So, it should be possible to search for these cocoon signatures for a larger sample of events without relying on the detection of an LLGRB. For events with detected cocoon emission, the long-term radio light curve is crucial for distinguishing between off-axis and choked jets.

We point out that based on estimated rates of GRBs and LLGRBs, the rate of off-axis GRBs in the local universe ($z < 0.05$) is only 1 order of magnitude smaller than the rate of LLGRBs (Soderberg et al. 2006; Liang et al. 2007), which are detected routinely (if infrequently, see the discussion below regarding why). The estimated rate of on-axis GRBs at $z = 0$ is $0.42^{+0.90}_{-0.40}$ yr^{-1} Gpc^{-3}, as measured from the Swift sample of classical GRBs (Lien et al. 2014). Taking a beaming fraction of 0.01 (Guetta et al. 2005), the expectation is for two (and up to six) GRBs in the local universe per year. Recently, Law et al. (2018) identified a candidate off-axis GRB afterglow in data from the VLA Sky Survey. Their estimate of the rate of events similar to this off-axis candidate is consistent with the expected off-axis GRB rate in the local universe.

Unfortunately, bursts like LLGRB 060218 are difficult to detect with ongoing GRB satellites, which are tuned to finding cosmological GRBs. First, the low luminosity ($L_{iso} = 2.6 \times 10^{46}$ erg s^{-1}) means that an LLGRB like 060218 can only be detected in the nearby universe. Second, the long timescale ($T_{90} = 2100$ s) makes it difficult to detect the event above the background evolution of wide-field detectors. Third, the low peak energy ($E_{pk} = 5$ keV) means that the burst is at the bottom of the energy range for sensitive wide-field detectors like Fermi/GBM and the IPN (Hurley et al. 2010). Finally, the fact that a burst like 060218 would only be detected in the local universe means that the number N detectable above a flux threshold S goes as $\log(N > S) \propto S^{-3/2}$; the number detected is very sensitive to the

Ho et al.

threshold used. Going forward, it would be useful to have a wide-field mission optimized for the detection of low-luminosity, long-duration bursts that peak in the soft X-ray band.

Due to the low LLGRB discovery rate and the small sample size, the LLGRB rate is highly uncertain; it is currently roughly consistent with the rate of Ic-BL SNe (Li et al. 2011; Kelly & Kirshner 2012). An outstanding question is therefore whether all Ic-BL SNe harbor an LLGRB. The effort to answer this question has been led by radio follow-up observations: by following up dozens of Ic-BL SNe found in wide-field optical surveys, Corsi et al. (2016) limited the fraction harboring SN 1998bw–like radio emission to $\lesssim 14\%$ (Corsi et al. 2016). However, as shown in Figure 13, SN 1998bw was the most radio-luminous LLGRB SN. Radio observations have generally not been sensitive enough to rule out a radio counterpart like that accompanying SN 2006aj.

High-cadence optical surveys provide a novel opportunity to measure the rate of Ic-BL SNe that are similar to SN 2006aj. Optical shock-cooling emission is expected to be isotropic and should not depend on the explosion properties that determine the second peak (ejecta mass, nickel mass). From the events in the ZTF with early high-cadence light curves, it appears that SN 2006aj–like events are uncommon, but more events will be needed to measure a robust rate.

Appendix A
Photometry Table

In Table A1, we provide the complete UVOIR photometry for SN 2020bvc.

Table A1
UVOIR Photometry for SN 2020bvc, Corrected for Milky Way Extinction,
with Epochs Given in the Observer Frame since t_0 (Defined in Section 2.1)

Date (MJD)	Δt (days)	Inst.	Filter	Mag (AB)
58,883.3406	0.67	P48+ZTF	i	17.44 ± 0.05
58,883.3901	0.72	P48+ZTF	i	17.46 ± 0.04
58,883.4763	0.81	P48+ZTF	g	16.82 ± 0.04
58,883.4966	0.83	P48+ZTF	g	16.83 ± 0.05
58,883.524	0.85	P48+ZTF	r	17.19 ± 0.04
58,884.0245	1.35	Swift+UVOT	$UVW1$	17.15 ± 0.01
58,884.0253	1.36	Swift+UVOT	U	17.08 ± 0.01
58,884.0257	1.36	Swift+UVOT	B	17.23 ± 0.01
58,884.0268	1.36	Swift+UVOT	$UVW2$	17.90 ± 0.01
58,884.028	1.36	Swift+UVOT	V	17.12 ± 0.01
58,884.0297	1.36	Swift+UVOT	$UVM2$	17.39 ± 0.01
58,884.1362	1.47	LT+IO:O	g	17.30 ± 0.01
58,884.3634	1.69	P60+SEDM	i	17.50 ± 0.03
58,884.3889	1.72	P48+ZTF	i	17.66 ± 0.05
58,884.4109	1.74	P48+ZTF	i	17.63 ± 0.04
58,884.4212	1.75	P48+ZTF	g	17.40 ± 0.06
58,884.469	1.8	P48+ZTF	g	17.38 ± 0.05
58,884.4754	1.81	P48+ZTF	g	17.37 ± 0.05
58,884.5473	1.88	P48+ZTF	r	17.58 ± 0.06
58,884.5533	1.88	P48+ZTF	r	17.57 ± 0.04
58,885.3891	2.72	P48+ZTF	i	17.67 ± 0.06
58,885.4111	2.74	P48+ZTF	i	17.65 ± 0.04
58,885.429	2.76	P48+ZTF	g	17.40 ± 0.05
58,885.4774	2.81	P48+ZTF	g	17.44 ± 0.07
58,885.5211	2.85	P48+ZTF	r	17.51 ± 0.04
58,885.538	2.87	P48+ZTF	r	17.52 ± 0.05
58,885.5533	2.88	Swift+UVOT	$UVW1$	19.48 ± 0.01
58,885.554	2.88	Swift+UVOT	U	18.33 ± 0.01
58,885.5543	2.88	Swift+UVOT	B	17.48 ± 0.01
58,885.5553	2.89	Swift+UVOT	$UVW2$	20.03 ± 0.01
58,885.5563	2.89	Swift+UVOT	V	17.19 ± 0.01
58,885.5577	2.89	Swift+UVOT	$UVM2$	20.30 ± 0.01
58,886.3926	3.72	P48+ZTF	i	17.52 ± 0.04
58,886.4112	3.74	P48+ZTF	i	17.52 ± 0.03
58,886.4337	3.76	P60+SEDM	r	17.20 ± 0.01
58,886.4354	3.77	P60+SEDM	g	17.34 ± 0.02
58,886.437	3.77	P60+SEDM	i	17.47 ± 0.01
58,886.4768	3.81	P48+ZTF	g	17.29 ± 0.04
58,886.4809	3.81	Swift+UVOT	$UVW1$	19.17 ± 0.01
58,886.4816	3.81	Swift+UVOT	U	18.17 ± 0.01
58,886.4819	3.81	Swift+UVOT	B	17.55 ± 0.01
58,886.4829	3.81	Swift+UVOT	$UVW2$	20.05 ± 0.01
58,886.4839	3.81	Swift+UVOT	V	17.55 ± 0.01
58,886.4854	3.82	Swift+UVOT	$UVM2$	20.87 ± 0.01
58,886.4941	3.82	P48+ZTF	g	17.29 ± 0.05
58,886.5229	3.85	P48+ZTF	r	17.29 ± 0.05
58,886.5506	3.88	P48+ZTF	r	17.33 ± 0.04
58,887.2802	4.61	Swift+UVOT	$UVW1$	19.48 ± 0.01
58,887.2808	4.61	Swift+UVOT	U	17.94 ± 0.01
58,887.2812	4.61	Swift+UVOT	B	17.54 ± 0.01
58,887.2821	4.61	Swift+UVOT	$UVW2$	20.47 ± 0.01
58,887.2829	4.61	Swift+UVOT	V	17.10 ± 0.01
58,887.2842	4.61	Swift+UVOT	$UVM2$	20.63 ± 0.01
58,887.3208	4.65	P48+ZTF	i	17.33 ± 0.05
58,887.429	4.76	P48+ZTF	g	17.07 ± 0.04
58,887.468	4.8	P48+ZTF	g	17.10 ± 0.05
58,887.4751	4.81	P48+ZTF	g	17.10 ± 0.05
58,887.5039	4.83	P48+ZTF	r	17.07 ± 0.05
58,887.5305	4.86	P48+ZTF	r	17.08 ± 0.05
58,887.5314	4.86	P48+ZTF	r	17.05 ± 0.04
58,888.3553	5.69	P60+SEDM	r	16.81 ± 0.02
58,888.357	5.69	P60+SEDM	g	16.98 ± 0.03
58,888.36	5.69	P48+ZTF	i	17.16 ± 0.04

Table A1
(Continued)

Date (MJD)	Δt (days)	Inst.	Filter	Mag (AB)
58,888.3928	5.72	P48+ZTF	i	17.14 ± 0.05
58,888.4746	5.8	P48+ZTF	r	16.88 ± 0.04
58,888.4892	5.82	P48+ZTF	r	16.87 ± 0.05
58,888.5373	5.87	P48+ZTF	g	16.92 ± 0.05
58,888.9397	6.27	Swift+UVOT	$UVW1$	19.06 ± 0.01
58,888.9404	6.27	Swift+UVOT	U	18.29 ± 0.01
58,888.9408	6.27	Swift+UVOT	B	17.09 ± 0.01
58,888.9418	6.27	Swift+UVOT	$UVW2$	20.72 ± 0.01
58,888.9428	6.27	Swift+UVOT	V	17.08 ± 0.01
58,888.9444	6.27	Swift+UVOT	$UVM2$	20.37 ± 0.01
58,890.3717	7.7	P48+ZTF	i	16.93 ± 0.03
58,890.3941	7.72	P48+ZTF	i	16.94 ± 0.03
58,890.4565	7.79	P48+ZTF	r	16.65 ± 0.04
58,890.4747	7.8	P48+ZTF	r	16.62 ± 0.06
58,890.4756	7.81	P48+ZTF	r	16.62 ± 0.04
58,890.5276	7.86	P48+ZTF	g	16.74 ± 0.05
58,890.5588	7.89	P48+ZTF	g	16.75 ± 0.05
58,890.5597	7.89	P48+ZTF	g	16.75 ± 0.05
58,891.3937	8.72	P48+ZTF	i	16.84 ± 0.03
58,891.4157	8.75	P48+ZTF	i	16.88 ± 0.03
58,891.4552	8.79	P48+ZTF	g	16.71 ± 0.04
58,891.4626	8.79	P48+ZTF	g	16.70 ± 0.04
58,891.7595	9.09	Swift+UVOT	$UVW1$	19.49 ± 0.01
58,891.7608	9.09	Swift+UVOT	U	18.22 ± 0.01
58,891.7615	9.09	Swift+UVOT	B	17.02 ± 0.01
58,891.7634	9.09	Swift+UVOT	$UVW2$	20.37 ± 0.01
58,891.7654	9.1	Swift+UVOT	V	16.44 ± 0.01
58,891.7683	9.1	Swift+UVOT	$UVM2$	20.77 ± 0.01
58,892.3651	9.7	P48+ZTF	g	16.68 ± 0.05
58,892.3832	9.71	P48+ZTF	g	16.69 ± 0.04
58,892.4559	9.79	P48+ZTF	i	16.83 ± 0.03
58,892.5181	9.85	P48+ZTF	r	16.46 ± 0.04
58,892.534	9.86	P48+ZTF	r	16.45 ± 0.04
58,893.3186	10.65	Swift+UVOT	$UVW2$	20.06 ± 0.01
58,893.4023	10.73	P48+ZTF	i	16.80 ± 0.03
58,893.4715	10.8	P48+ZTF	g	16.67 ± 0.04
58,893.4965	10.83	P48+ZTF	g	16.67 ± 0.04
58,893.4974	10.83	P48+ZTF	g	16.67 ± 0.04
58,893.521	10.85	P48+ZTF	r	16.41 ± 0.04
58,893.53	10.86	Swift+UVOT	V	16.49 ± 0.01
58,893.5325	10.86	Swift+UVOT	$UVM2$	20.90 ± 0.01
58,893.5338	10.86	P48+ZTF	r	16.43 ± 0.03
58,893.7579	11.09	Swift+UVOT	$UVW1$	19.63 ± 0.01
58,893.759	11.09	Swift+UVOT	U	18.40 ± 0.01
58,893.7595	11.09	Swift+UVOT	B	17.11 ± 0.01
58,893.7604	11.09	Swift+UVOT	$UVW2$	20.43 ± 0.01
58,894.3388	11.67	P48+ZTF	g	16.68 ± 0.04
58,894.4351	11.77	P48+ZTF	i	16.75 ± 0.03
58,894.4554	11.79	P48+ZTF	i	16.74 ± 0.03
58,894.5153	11.85	P48+ZTF	r	16.38 ± 0.04
58,894.535	11.87	P48+ZTF	r	16.37 ± 0.04
58,894.5468	11.88	P48+ZTF	g	16.70 ± 0.03
58,895.137	12.47	Swift+UVOT	$UVW1$	19.89 ± 0.01
58,895.1377	12.47	Swift+UVOT	U	18.63 ± 0.01
58,895.138	12.47	Swift+UVOT	B	17.35 ± 0.01
58,895.1391	12.47	Swift+UVOT	$UVW2$	20.41 ± 0.01
58,895.14	12.47	Swift+UVOT	V	16.35 ± 0.01
58,895.1417	12.47	Swift+UVOT	$UVM2$	20.97 ± 0.01
58,895.4968	12.83	P48+ZTF	r	16.35 ± 0.03
58,895.4972	12.83	P48+ZTF	r	16.33 ± 0.04
58,896.3318	13.66	P48+ZTF	i	16.72 ± 0.03
58,896.3934	13.72	P48+ZTF	i	16.70 ± 0.03
58,898.1568	15.49	LT+IO:O	r	16.32 ± 0.02
58,898.1576	15.49	LT+IO:O	i	16.76 ± 0.02

Table A1
(Continued)

Date (MJD)	Δt (days)	Inst.	Filter	Mag (AB)
58,898.1585	15.49	LT+IO:O	g	16.75 ± 0.02
58,898.1593	15.49	LT+IO:O	u	18.66 ± 0.04
58,898.445	15.77	P48+ZTF	g	16.92 ± 0.04
58,898.4558	15.79	P48+ZTF	g	16.90 ± 0.03
58,898.4955	15.83	P48+ZTF	r	16.38 ± 0.03
58,898.5119	15.84	P48+ZTF	r	16.39 ± 0.04
58,898.5128	15.84	P48+ZTF	r	16.35 ± 0.03
58,898.5335	15.86	P48+ZTF	r	16.36 ± 0.03
58,898.5463	15.88	P48+ZTF	g	16.93 ± 0.04
58,899.4051	16.74	P48+ZTF	g	16.92 ± 0.04
58,899.4351	16.77	P48+ZTF	g	16.94 ± 0.04
58,899.4828	16.81	P48+ZTF	r	16.34 ± 0.04
58,899.5057	16.84	P48+ZTF	r	16.36 ± 0.03
58,899.5302	16.86	P48+ZTF	g	16.95 ± 0.05
58,900.3929	17.72	P48+ZTF	g	16.98 ± 0.05
58,900.4467	17.78	P48+ZTF	r	16.26 ± 0.04
58,900.4499	17.78	P60+SEDM	r	16.38 ± 0.01
58,900.4516	17.78	P60+SEDM	g	16.98 ± 0.02
58,900.4532	17.78	P60+SEDM	i	16.64 ± 0.02
58,900.4787	17.81	P48+ZTF	r	16.35 ± 0.03
58,900.4938	17.82	P48+ZTF	r	16.34 ± 0.04
58,900.5289	17.86	P48+ZTF	g	16.98 ± 0.07
58,901.4137	18.74	P48+ZTF	r	16.38 ± 0.03
58,901.4335	18.76	P48+ZTF	r	16.39 ± 0.03
58,901.4546	18.78	P48+ZTF	r	16.37 ± 0.03
58,901.4546	18.78	P48+ZTF	r	16.37 ± 0.03
58,902.6701	20.0	Swift+UVOT	UVW1	20.56 ± 0.01
58,902.6715	20.0	Swift+UVOT	U	19.52 ± 0.01
58,902.6725	20.0	Swift+UVOT	B	17.82 ± 0.01
58,902.6748	20.0	Swift+UVOT	UVW2	20.22 ± 0.01
58,902.6772	20.01	Swift+UVOT	V	16.49 ± 0.01
58,902.6791	20.01	Swift+UVOT	UVM2	22.23 ± 0.01
58,903.36	20.69	P48+ZTF	g	17.21 ± 0.06
58,903.412	20.74	P48+ZTF	r	16.48 ± 0.03
58,903.4217	20.75	P48+ZTF	r	16.45 ± 0.03
58,903.4571	20.79	P48+ZTF	r	16.48 ± 0.03
58,903.4605	20.79	P48+ZTF	r	16.46 ± 0.05
58,903.4953	20.83	P48+ZTF	r	16.47 ± 0.03
58,903.4962	20.83	P48+ZTF	r	16.51 ± 0.04
58,903.5079	20.84	P48+ZTF	r	16.45 ± 0.04
58,903.5409	20.87	P48+ZTF	g	17.22 ± 0.05
58,904.3954	21.73	P48+ZTF	i	16.79 ± 0.03
58,904.4029	21.73	P48+ZTF	i	16.81 ± 0.02
58,904.4461	21.78	P48+ZTF	g	17.28 ± 0.05
58,904.489	21.82	P48+ZTF	r	16.50 ± 0.03
58,906.3392	23.67	P48+ZTF	g	17.44 ± 0.05
58,906.4339	23.76	P48+ZTF	i	16.89 ± 0.02
58,906.4868	23.82	P48+ZTF	r	16.56 ± 0.04
58,906.4878	23.82	P48+ZTF	r	16.57 ± 0.03
58,906.5057	23.84	P48+ZTF	r	16.57 ± 0.03
58,906.5381	23.87	P48+ZTF	g	17.41 ± 0.05
58,906.539	23.87	P48+ZTF	g	17.45 ± 0.06
58,906.5551	23.89	P48+ZTF	i	16.88 ± 0.04
58,908.3226	25.65	Swift+UVOT	UVW1	19.63 ± 0.01
58,908.3236	25.65	Swift+UVOT	U	20.53 ± 0.01
58,908.3243	25.65	Swift+UVOT	B	18.19 ± 0.01
58,908.3259	25.66	Swift+UVOT	UVW2	20.45 ± 0.01
58,908.3275	25.66	Swift+UVOT	V	16.99 ± 0.01
58,908.3288	25.66	Swift+UVOT	UVM2	21.54 ± 0.01
58,908.4122	25.74	P48+ZTF	i	16.98 ± 0.03
58,908.4158	25.75	P60+SEDM	r	16.77 ± 0.02
58,908.4258	25.76	P48+ZTF	i	16.99 ± 0.03
58,908.4624	25.79	P48+ZTF	r	16.73 ± 0.04

Date (MJD)	Δt (days)	Inst.	Filter	Mag (AB)
58,908.4949	25.82	P48+ZTF	r	16.76 ± 0.04
58,908.5315	25.86	P48+ZTF	g	17.46 ± 0.09
58,908.5565	25.89	P48+ZTF	g	17.45 ± 0.05
58,909.175	26.5	LT+IO:O	r	16.75 ± 0.02
58,909.1758	26.51	LT+IO:O	i	17.03 ± 0.02
58,909.1766	26.51	LT+IO:O	g	17.54 ± 0.02
58,909.1775	26.51	LT+IO:O	u	19.98 ± 0.07
58,909.1789	26.51	LT+IO:O	z	16.66 ± 0.01
58,911.2535	28.58	P48+ZTF	i	17.07 ± 0.05
58,911.3516	28.68	P48+ZTF	i	17.14 ± 0.03
58,911.4256	28.76	P48+ZTF	g	17.85 ± 0.06
58,911.4265	28.76	P48+ZTF	g	17.89 ± 0.07
58,911.4766	28.81	P48+ZTF	r	16.87 ± 0.04
58,911.4826	28.81	P48+ZTF	r	16.87 ± 0.04
58,911.4836	28.81	P48+ZTF	r	16.85 ± 0.04
58,911.551	28.88	P48+ZTF	g	17.85 ± 0.07
58,911.5515	28.88	P48+ZTF	g	17.81 ± 0.08
58,911.5533	28.88	P48+ZTF	g	17.73 ± 0.07
58,911.5538	28.88	P48+ZTF	g	17.79 ± 0.06
58,912.1515	29.48	LT+IO:O	r	16.94 ± 0.02
58,912.1523	29.48	LT+IO:O	i	17.21 ± 0.02
58,912.1532	29.48	LT+IO:O	g	17.75 ± 0.01
58,912.154	29.48	LT+IO:O	u	20.15 ± 0.10
58,912.1554	29.49	LT+IO:O	z	16.81 ± 0.02
58,912.3746	29.7	P48+ZTF	i	17.19 ± 0.03
58,912.3792	29.71	P48+ZTF	i	17.16 ± 0.04
58,912.4747	29.8	P48+ZTF	r	16.95 ± 0.04
58,912.4973	29.83	P48+ZTF	r	16.96 ± 0.04
58,912.5209	29.85	P48+ZTF	g	17.93 ± 0.08
58,912.5468	29.88	P48+ZTF	g	17.94 ± 0.07

(This table is available in machine-readable form.)

Appendix B
Details: Mass and Radius of the Extended Material

This calculation closely follows that of Nakar & Piro (2014) and Kasen (2017).

Assume that the layer undergoing shock cooling has mass M_e and radius R_e. Photons diffuse from this layer on a timescale $t_{\rm diff} \sim \tau R_e/c$. The layer itself is moving at a characteristic velocity v_e; the timescale of expanding is $t_{\rm exp} \sim R_e/v_e$. The bulk of the photons emerge from the layer where $\tau R_e/c \sim R_e/c$, or $\tau \sim c/v_e$.

At a given radius, the optical depth τ drops due to expansion; $\tau \sim \kappa \rho R$, where $\rho \sim M_e/(4\pi R^3/3)$. The radius increases as $R \sim v_e t$, so we find that $\tau \sim 3\kappa M_e/(4\pi(v_e t)^2)$. Setting this equal to c/v_e,

$$t \sim \left(\frac{3}{4\pi} \frac{\kappa M_e}{v_e c} \right)^{1/2}. \tag{B1}$$

For SN 2020bvc, we have an upper limit on the time to peak of $t_p \lesssim 1$ days. From the spectra, we estimate $v_e \sim 0.1c$. We take $\kappa = 0.2$ cm^{-2} g^{-1} for a hydrogen-poor gas. Altogether, we find $M_e \sim 10^{-2} M_\odot$. Note that this is an upper limit, because the rise time was likely much faster than what we could measure. So, we conclude that $M_e < 10^{-2} M_\odot$.

Next, we estimate R_e. We assume that the shock deposits energy $E_{\rm dep}$ into the layer. Then the layer cools from expansion,

$E_{\rm cool} \sim E_{\rm dep}(R_e/v_e t)$. The luminosity from cooling is $L_{\rm cool} \sim E_{\rm cool}/t_{\rm cool} \sim E_{\rm dep} R_0/v_e t^2$.

Assuming that the deposited energy is half the kinetic energy $E_{\rm KE}$ of the shock, $E_{\rm dep} \sim E_{\rm KE}/2 = \pi R_e^2 dR \rho v_s^2$, where dR and ρ are the width and density of the layer. Taking $dR \approx R_e$ and $\rho \sim M_e/(4\pi R_e^2 dR)$, we find $E_{\rm dep} \sim v_e^2 M_e/4$. So, our expression for the luminosity is

$$L_{\rm cool} \sim \frac{v_e R_e M_e}{4t^2}. \qquad (B2)$$

Taking $M_e < 10^{-2} M_\odot$, $t < 1$ days, $v_e = 0.1c$, and $L > 10^{43}$ erg s^{-1}, we find $R_e > 10^{12}$ cm. We can only measure a lower limit on the radius because the true peak luminosity is likely much higher than what we can measure.

Appendix C
Details: Properties of the Forward Shock

The framework described in Chevalier (1998) assumes that the radio emission arises from a population of relativistic electrons with Lorentz factors that follow a power law of index p down to a cutoff γ_m,

$$\frac{dN(\gamma_e)}{d\gamma_e} \propto \gamma_e^{-p}, \gamma \geqslant \gamma_m, \qquad (C1)$$

where $2.3 \lesssim p \lesssim 3$ (Jones & Ellison 1991; Pelletier et al. 2017). The expression for the typical electron Lorentz factor γ_m is

$$\gamma_m - 1 \approx \epsilon_e \frac{m_p v^2}{m_e c^2}, \qquad (C2)$$

where ϵ_e is the fraction of energy in relativistic electrons, m_p is the proton mass, v is the shock velocity, m_e is the electron mass, and c is the speed of light.

The resulting spectrum is a broken power law where $\nu^{5/2}$ at $\nu < \nu_a$, $\nu^{-(p-1)/2}$ at $\nu > \nu_a$, and ν_a is called the self-absorption frequency (Rybicki & Lightman 1986). By observing the peak frequency ν_p and peak flux F_p and assuming that $\nu_p = \nu_a$, we can estimate the outer shock radius R_p and magnetic field strength B_p. We take $p = 3$ (the results do not depend strongly on the value of p) and a filling factor $f = 0.5$ and assume equipartition ($\alpha = \epsilon_e/\epsilon_B = 1$, where ϵ_e/ϵ_B is the ratio of the energy density in relativistic electrons to the energy density in magnetic fields).

Assuming that the radio emission is dominated by the transient, we have an upper limit on the peak frequency of $\nu_p < 3$ GHz and a lower limit on the peak flux density of $F_p > 113 \, \mu$Jy at $\Delta t = 24$ days. We use Equations (13) and (14) of Chevalier (1998) to solve for R and B and find $R > 1.7 \times 10^{16}$ cm, $B < 0.34$ G, and a mean shock velocity up to 13 days of $v > 0.3c$. Expressions for the total energy thermalized by the shock U and ambient density n_e are given in Ho et al. (2019b, hereafter H19) following the same framework as in Chevalier (1998). Using Equation (12) in H19 and taking $\epsilon_B = 1/3$, we find $U = 1.3 \times 10^{47}$ erg. Using Equation (16) in H19, we find $n_e \approx 160$ cm^{-3}, which corresponds to a mass-loss rate (Equation (23) of H19) of

$$\frac{\dot{M}}{v_w}\left(\frac{1000 \text{ km s}^{-1}}{10^{-4} M_\odot \text{ yr}^{-1}}\right) = 0.2, \qquad (C3)$$

where v_w is the wind velocity.

The cooling frequency is defined as

$$\nu_c = \gamma_c^2 \nu_g, \qquad (C4)$$

where

$$\gamma_c = \frac{6\pi m_e c}{\sigma_T B^2 t} \qquad (C5)$$

and

$$\nu_g = \frac{q_e B}{2\pi m_e c}. \qquad (C6)$$

Combining Equations (C4), (C5), and (C6), we have

$$\nu_c = \frac{18\pi m_e c q_e}{\sigma_T^2 B^3 t^2} \approx 1.0 \times 10^{13} \text{ GHz}. \qquad (C7)$$

Finally, we find that the bulk of the electrons have a Lorentz factor $\gamma_m = 22$.

Appendix D
Inverse Compton Scattering

The luminosity from inverse Compton scattering of optical photons from the relativistic electrons is

$$\frac{L_{\rm IC}}{L_{\rm syn}} = \frac{u_{ph}}{u_B}, \qquad (D1)$$

where $u_{\rm ph}$ is the photon energy density (which we measure from our UVOIR observations) and u_B is the magnetic energy density (which we measure from our radio observations; Rybicki & Lightman 1986). Taking $R_{\rm ph} = 2 \times 10^{14}$ cm and $L_{\rm bol} > 2 \times 10^{42}$ erg s^{-1}, we have

$$u_{ph} = \frac{L_{\rm bol}}{4\pi R^3/3} > 0.07 \text{ erg cm}^{-3}. \qquad (D2)$$

Using $B < 0.34$ G, we have

$$u_B = \frac{B^2}{8\pi} < 0.005 \text{ erg cm}^{-3}. \qquad (D3)$$

So, the dominant cooling mechanism is inverse Compton scattering rather than synchrotron radiation, and $L_{\rm IC}$ is an order of magnitude greater than $L_{\rm syn}$ (the radio luminosity). Photons emitted at frequency ν_0 that are upscattered by electrons at γ_m will emerge with an average frequency $\nu_{\rm IC}$, where

$$\langle \nu_{\rm IC} \rangle = \frac{4}{3}\gamma_m^2 \nu_0. \qquad (D4)$$

ORCID iDs

Anna Y. Q. Ho https://orcid.org/0000-0002-9017-3567
S. R. Kulkarni https://orcid.org/0000-0001-5390-8563
Daniel A. Perley https://orcid.org/0000-0001-8472-1996
S. Bradley Cenko https://orcid.org/0000-0003-1673-970X
Alessandra Corsi https://orcid.org/0000-0001-8104-3536
Steve Schulze https://orcid.org/0000-0001-6797-1889
Ragnhild Lunnan https://orcid.org/0000-0001-9454-4639
Jesper Sollerman https://orcid.org/0000-0003-1546-6615
Avishay Gal-Yam https://orcid.org/0000-0002-3653-5598
Cristina Barbarino https://orcid.org/0000-0002-3821-6144
Rachel J. Bruch https://orcid.org/0000-0001-8208-2473
Eric Burns https://orcid.org/0000-0001-8018-5348

Richard Dekany ⓘ https://orcid.org/0000-0002-5884-7867
Dmitry A. Duev ⓘ https://orcid.org/0000-0001-5060-8733
Dmitry D. Frederiks ⓘ https://orcid.org/0000-0002-1153-6340
Christoffer Fremling ⓘ https://orcid.org/0000-0002-4223-103X
Daniel A. Goldstein ⓘ https://orcid.org/0000-0003-3461-8661
V. Zach Golkhou ⓘ https://orcid.org/0000-0001-8205-2506
Matthew J. Graham ⓘ https://orcid.org/0000-0002-3168-0139
Mansi M. Kasliwal ⓘ https://orcid.org/0000-0002-5619-4938
Thomas Kupfer ⓘ https://orcid.org/0000-0002-6540-1484
Russ R. Laher ⓘ https://orcid.org/0000-0003-2451-5482
Julia Martikainen ⓘ https://orcid.org/0000-0003-2211-4001
Frank J. Masci ⓘ https://orcid.org/0000-0002-8532-9395
Ben Rusholme ⓘ https://orcid.org/0000-0001-7648-4142
Volodymyr Savchenko ⓘ https://orcid.org/0000-0001-6353-0808
David L. Shupe ⓘ https://orcid.org/0000-0003-4401-0430
Maayane T. Soumagnac ⓘ https://orcid.org/0000-0001-6753-1488
Nora L. Strotjohann ⓘ https://orcid.org/0000-0002-4667-6730
Dmitry S. Svinkin ⓘ https://orcid.org/0000-0002-2208-2196
Leonardo Tartaglia ⓘ https://orcid.org/0000-0003-3433-1492
Lin Yan ⓘ https://orcid.org/0000-0003-1710-9339

References

Aptekar, R. L., Frederiks, D. D., Golenetskii, S. V., et al. 1995, SSRv, 71, 265
Arcavi, I., Gal-Yam, A., Yaron, O., et al. 2011, ApJL, 742, L18
Arnett, W. D. 1982, ApJ, 253, 785
Astropy Collaboration, Price-Whelan, A. M., Sipőcz, B. M., et al. 2018, AJ, 156, 123
Astropy Collaboration, Robitaille, T. P., Tollerud, E. J., et al. 2013, A&A, 558, A33
Barnes, J., Duffell, P. C., Liu, Y., et al. 2018, ApJ, 860, 38
Barnsley, R. M., Smith, R. J., & Steele, I. A. 2012, AN, 333, 101
Barthelmy, S. D., Barbier, L. M., Cummings, J. R., et al. 2005, SSRv, 120, 143
Bellm, E. C., Kulkarni, S. R., Barlow, T., et al. 2019a, PASP, 131, 068003
Bellm, E. C., Kulkarni, S. R., Graham, M. J., et al. 2019b, PASP, 131, 018002
Bellm, E. C., & Sesar, B. 2016, pyraf-dbsp: Reduction pipeline for the Palomar Double Beam Spectrograph, Astrophysics Source Code Library, ascl:1602.002
Bersier, D., Fruchter, A. S., Strolger, L. G., et al. 2006, ApJ, 643, 284
Bersten, M. C., Benvenuto, O. G., Nomoto, K., et al. 2012, ApJ, 757, 31
Bersten, M. C., Folatelli, G., García, F., et al. 2018, Natur, 554, 497
Bianco, F. B., Modjaz, M., Hicken, M., et al. 2014, ApJS, 213, 19
Blackburn, J. K., Shaw, R. A., Payne, H. E., Hayes, J. J. E., & Heasarc 1999, FTOOLS: A general package of software to manipulate FITS files, Astrophysics Source Code Library, ascl:9912.002
Blagorodnova, N., Neill, J. D., Walters, R., et al. 2018, PASP, 130, 035003
Blanton, M. R., Kazin, E., Muna, D., Weaver, B. A., & Price-Whelan, A. 2011, AJ, 142, 31
Brown, P. J., Breeveld, A. A., Holland, S., Kuin, P., & Pritchard, T. 2014, Ap&SS, 354, 89
Brown, T. M., Baliber, N., Bianco, F. B., et al. 2013, PASP, 125, 1031
Bufano, F., Pian, E., Sollerman, J., et al. 2012, ApJ, 753, 67
Burrows, D. N., Hill, J. E., Nousek, J. A., et al. 2005, SSRv, 120, 165
Campana, S., Mangano, V., Blustin, A. J., et al. 2006, Natur, 442, 1008
Cano, Z. 2013, MNRAS, 434, 1098
Cano, Z., Bersier, D., Guidorzi, C., et al. 2011, ApJ, 740, 41
Cano, Z., Wang, S.-Q., Dai, Z.-G., & Wu, X.-F. 2017, AdAst, 2017, 8929054
Cantiello, M., Yoon, S. C., Langer, N., & Livio, M. 2007, A&A, 465, L29
Cenko, S. B., Fox, D. B., Moon, D.-S., et al. 2006, PASP, 118, 1396
Cenko, S. B., Kulkarni, S. R., Horesh, A., et al. 2013, ApJ, 769, 130
Chambers, K. C., Magnier, E. A., Metcalfe, N., et al. 2016, arXiv:1612.05560
Chang, Y.-Y., van der Wel, A., da Cunha, E., & Rix, H.-W. 2015, ApJS, 219, 8
Chevalier, R. A. 1998, ApJ, 499, 810
Chevalier, R. A. 2012, ApJL, 752, L2
Chevalier, R. A., & Fransson, C. 2006, ApJ, 651, 381
Chevalier, R. A., & Fransson, C. 2008, ApJL, 683, L135
Clocchiatti, A., Suntzeff, N. B., Covarrubias, R., & Candia, P. 2011, AJ, 141, 163
Corsi, A., Cenko, S. B., Kasliwal, M. M., et al. 2017, ApJ, 847, 54
Corsi, A., Gal-Yam, A., Kulkarni, S. R., et al. 2016, ApJ, 830, 42
De, K., Kasliwal, M. M., Ofek, E. O., et al. 2018, Sci, 362, 201
De, K., Kasliwal, M. M., Tzanidakis, A., et al. 2019, arXiv:2004.09029

Dekany, R., Smith, R. M., Riddle, R., et al. 2020, PASP, 132, 038001
D'Elia, V., Campana, S., D'Aì, A., et al. 2018, A&A, 619, A66
Dey, A., Schlegel, D. J., Lang, D., et al. 2019, AJ, 157, 168
Djupvik, A. A., & Andersen, J. 2010, ASSP, 14, 211
Duev, D. A., Mahabal, A., Masci, F. J., et al. 2019, MNRAS, 489, 3582
Eldridge, J. J., Langer, N., & Tout, C. A. 2011, MNRAS, 414, 3501
Evans, P. A., Beardmore, A. P., Page, K. L., et al. 2007, A&A, 469, 379
Evans, P. A., Beardmore, A. P., Page, K. L., et al. 2009, MNRAS, 397, 1177
Fan, Y.-Z., Piran, T., & Xu, D. 2006, JCAP, 2006, 013
Fatkhullin, T. A., Sokolov, V. V., Moiseev, A. V., Guziy, S., & Castro-Tirado, A. J. 2006, GCN, 4809, 1
Ferrero, P., Kann, D. A., Zeh, A., et al. 2006, A&A, 457, 857
Fitzpatrick, E. L. 1999, PASP, 111, 63
Flewelling, H. A., Magnier, E. A., Chambers, K. C., et al. 2016, arXiv:1612.05243
Freeman, P., Nguyen, D., Doe, S., & Siemiginowska, A. 2011, Sherpa: CIAO Modeling and Fitting Package, Astrophysics Source Code Library, ascl:1107.005
Fremling, C., Sollerman, J., Taddia, F., et al. 2016, A&A, 593, A68
Fremling, U. C., Miller, A. A., Sharma, Y., et al. 2020, ApJ, 895, 32
Fruscione, A., McDowell, J. C., Allen, G. E., et al. 2006, Proc. SPIE, 6270, 62701V
Galama, T. J., Vreeswijk, P. M., van Paradijs, J., et al. 1998, Natur, 395, 670
Gal-Yam, A. 2017, in Observational and Physical Classification of Supernovae, ed. A. W. Alsabti & P. Murdin (Cham: Springer), 195
Gal-Yam, A., Arcavi, I., Ofek, E. O., et al. 2014, Natur, 509, 471
Gehrels, N., Chincarini, G., Giommi, P., et al. 2004, ApJ, 611, 1005
Graham, M. J., Kulkarni, S. R., Bellm, E. C., et al. 2019, PASP, 131, 078001
Granot, J., De Colle, F., & Ramirez-Ruiz, E. 2018, MNRAS, 481, 2711
Greiner, J., Michałowski, M. J., Klose, S., et al. 2016, A&A, 593, A17
Gruber, D., Goldstein, A., Weller von Ahlefeld, V., et al. 2014, ApJS, 211, 12
Guetta, D., Piran, T., & Waxman, E. 2005, ApJ, 619, 412
Hammer, F., Flores, H., Schaerer, D., et al. 2006, A&A, 454, 103
Hiramatsu, D., Arcavi, I., Burke, J., et al. 2020, Transient Name Server Classification Report, 2020-403, 1
HI4PI Collaboration, Ben Bekhti, N., Flöer, L., et al. 2016, A&A, 594, A116
Hjorth, J. 2013, RSPTA, 371, 20120275
Hjorth, J., & Bloom, J. S. 2012, The Gamma-Ray Burst—Supernova Connection (Cambridge: Cambridge Univ. Press), 169
Ho, A. Y. Q. 2020, Transient Name Server AstroNote, 42, 1
Ho, A. Y. Q., Cenko, B., Perley, D., Corsi, A., & Brightman, M. 2020a, Transient Name Server AstroNote, 45, 1
Ho, A., Corsi, A., & Cenko, S. B. 2020b, ApJ, 893, 132
Ho, A. Y. Q., Goldstein, D. A., Schulze, S., et al. 2019a, ApJ, 887, 169
Ho, A. Y. Q., Phinney, E. S., Ravi, V., et al. 2019b, ApJ, 871, 73
Ho, P. T. P., Moran, J. M., & Lo, K. Y. 2004, ApJL, 616, L1
Högbom, J. A. 1974, A&AS, 15, 417
Hunter, J. D. 2007, CSE, 9, 90
Hurley, K., Golenetskii, S., Aptekar, R., et al. 2010, in AIP Conf. Ser. 1279, Deciphering the Ancient Universe with Gamma-Ray Bursts, ed. N. Kawai & S. Nagataki (Melville, NY: AIP), 330
Irwin, C. M., & Chevalier, R. A. 2016, MNRAS, 460, 1680
Iwamoto, K., Mazzali, P. A., Nomoto, K., et al. 1998, Natur, 395, 672
Izzo, L., Auchettl, K., Hjorth, J., et al. 2020, A&A, 639, L11
Izzo, L., de Ugarte Postigo, A., Maeda, K., et al. 2019, Natur, 565, 324
Jones, F. C., & Ellison, D. C. 1991, SSRv, 58, 259
Kasen, D. 2017, in Unusual Supernovae and Alternative Power Sources, ed. A. W. Alsabti & P. Murdin (Cham: Springer), 939
Kasliwal, M. M., Cannella, C., Bagdasaryan, A., et al. 2019, PASP, 131, 038003
Kelly, P. L., & Kirshner, R. P. 2012, ApJ, 759, 107
Kraft, R. P., Burrows, D. N., & Nousek, J. A. 1991, ApJ, 374, 344
Kulkarni, S. R., Frail, D. A., Wieringa, M. H., et al. 1998, Natur, 395, 663
Laskar, T., Coppejans, D. L., Margutti, R., & Alexander, K. D. 2017, GCN, 22216, 1
Law, C. J., Gaensler, B. M., Metzger, B. D., Ofek, E. O., & Sironi, L. 2018, ApJL, 866, L22
Li, W., Leaman, J., Chornock, R., et al. 2011, MNRAS, 412, 1441
Liang, E., Zhang, B., Virgili, F., & Dai, Z. G. 2007, ApJ, 662, 1111
Lien, A., Sakamoto, T., Gehrels, N., et al. 2014, ApJ, 783, 24
Lupton, R., Blanton, M. R., Fekete, G., et al. 2004, PASP, 116, 133
Lyman, J. D., Bersier, D., James, P. A., et al. 2016, MNRAS, 457, 328
Mahabal, A., Rebbapragada, U., Walters, R., et al. 2019, PASP, 131, 038002
Margutti, R., Guidorzi, C., Lazzati, D., et al. 2015, ApJ, 805, 159
Margutti, R., Milisavljevic, D., Soderberg, A. M., et al. 2014, ApJ, 797, 107
Masci, F. J., Laher, R. R., Rusholme, B., et al. 2019, PASP, 131, 018003

Mazzali, P. A., Iwamoto, K., & Nomoto, K. 2000, ApJ, 545, 407
Mazzali, P. A., Valenti, S., Della Valle, M., et al. 2008, Sci, 321, 1185
McMullin, J. P., Waters, B., Schiebel, D., Young, W., & Golap, K. 2007, in ASP Conf. Ser. 376, CASA Architecture and Applications, ed. R. A. Shaw, F. Hill, & D. J. Bell (San Francisco, CA: ASP), 127
Meegan, C., Lichti, G., Bhat, P. N., et al. 2009, ApJ, 702, 791
Mirabal, N., Halpern, J. P., An, D., Thorstensen, J. R., & Terndrup, D. M. 2006, ApJL, 643, L99
Modjaz, M., Bianco, F. B., Siwek, M., et al. 2020, ApJ, 892, 153
Modjaz, M., Li, W., Butler, N., et al. 2009, ApJ, 702, 226
Modjaz, M., Liu, Y. Q., Bianco, F. B., & Graur, O. 2016, ApJ, 832, 108
Modjaz, M., Stanek, K. Z., Garnavich, P. M., et al. 2006, ApJL, 645, L21
Murphy, E. J., Condon, J. J., Schinnerer, E., et al. 2011, ApJ, 737, 67
Nakar, E. 2015, ApJ, 807, 172
Nakar, E., & Piro, A. L. 2014, ApJ, 788, 193
Narayana Bhat, P., Meegan, C. A., von Kienlin, A., et al. 2016, ApJS, 223, 28
Oke, J. B., Cohen, J. G., Carr, M., et al. 1995, PASP, 107, 375
Oke, J. B., & Gunn, J. E. 1982, PASP, 94, 586
Pelletier, G., Bykov, A., Ellison, D., & Lemoine, M. 2017, SSRv, 207, 319
Perley, D., Schulze, S., & Bruch, R. 2020, Transient Name Server AstroNote, 37, 1
Perley, D. A. 2019, PASP, 131, 084503
Perley, D. A., Cenko, S. B., Corsi, A., et al. 2014, ApJ, 781, 37
Perley, D. A., Schulze, S., & de Ugarte Postigo, A. 2017, GCN, 22252, 1
Perley, D. A., & Taggart, K. 2017, GCN, 22194, 1
Perley, R. A., Chandler, C. J., Butler, B. J., & Wrobel, J. M. 2011, ApJL, 739, L1
Pettini, M., & Pagel, B. E. J. 2004, MNRAS, 348, L59
Pian, E., Mazzali, P. A., Masetti, N., et al. 2006, Natur, 442, 1011
Piascik, A. S., Steele, I. A., Bates, S. D., et al. 2014, Proc. SPIE, 9147, 91478H
Piran, T. 2004, RvMP, 76, 1143
Piro, A. L. 2015, ApJL, 808, L51
Planck Collaboration, Ade, P. A. R., Aghanim, N., et al. 2016, A&A, 594, A13
Quataert, E., & Shiode, J. 2012, MNRAS Letters, 423, L92
Rigault, M., Neill, J. D., Blagorodnova, N., et al. 2019, A&A, 627, A115
Roming, P. W. A., Kennedy, T. E., Mason, K. O., et al. 2005, SSRv, 120, 95
Rybicki, G. B., & Lightman, A. P. 1986, Radiative Processes in Astrophysics (Weinheim: Wiley-VCH)
Sakamoto, T., Lamb, D. Q., Graziani, C., et al. 2004, ApJ, 602, 875
Sapir, N., & Waxman, E. 2017, ApJ, 838, 130
Sault, R. J., Teuben, P. J., & Wright, M. C. H. 1995, in ASP Conf. Ser. 77, A Retrospective View of MIRIAD, ed. R. A. Shaw, H. E. Payne, & J. J. E. Hayes (San Francisco, CA: ASP), 433
Schlafly, E. F., & Finkbeiner, D. P. 2011, ApJ, 737, 103
Shappee, B. J., Prieto, J. L., Grupe, D., et al. 2014, ApJ, 788, 48
Smith, N. 2014, ARA&A, 52, 487
Sobacchi, E., Granot, J., Bromberg, O., & Sormani, M. C. 2017, MNRAS, 472, 616
Soderberg, A. M., Chakraborti, S., Pignata, G., et al. 2010, Natur, 463, 513
Soderberg, A. M., Kulkarni, S. R., Berger, E., et al. 2004, ApJ, 606, 994
Soderberg, A. M., Kulkarni, S. R., Nakar, E., et al. 2006, Natur, 442, 1014
Sollerman, J., Holland, S. T., Challis, P., et al. 2002, A&A, 386, 944
Sollerman, J., Jaunsen, A. O., Fynbo, J. P. U., et al. 2006, A&A, 454, 503
Sollerman, J., Östlin, G., Fynbo, J. P. U., et al. 2005, NewA, 11, 103
Stanek, K. Z. 2020, Transient Name Server Discovery Report, 2020-381, 1
Steele, I. A., Smith, R. J., Rees, P. C., et al. 2004, Proc. SPIE, 5489, 679
Tachibana, Y., & Miller, A. A. 2018, PASP, 130, 128001
Taddia, F., Fremling, C., Sollerman, J., et al. 2016, A&A, 592, A89
Taddia, F., Sollerman, J., Fremling, C., et al. 2019, A&A, 621, A71
Taggart, K., & Perley, D. 2019, arXiv:1911.09112
Tonry, J. L., Denneau, L., Heinze, A. N., et al. 2018, PASP, 130, 064505
Valenti, S., Benetti, S., Cappellaro, E., et al. 2008, MNRAS, 383, 1485
van den Heuvel, E. P. J., & Portegies Zwart, S. F. 2013, ApJ, 779, 114
Virtanen, P., Gommers, R., Oliphant, T. E., et al. 2020, Nature Methods, 17, 261
von Kienlin, A., Meegan, C. A., Paciesas, W. S., et al. 2014, ApJS, 211, 13
Wang, J., Zhu, Z. P., Xu, D., et al. 2018, ApJ, 867, 147
Waxman, E., Mészáros, P., & Campana, S. 2007, ApJ, 667, 351
Whitesides, L., Lunnan, R., Kasliwal, M. M., et al. 2017, ApJ, 851, 107
Woosley, S. E., & Bloom, J. S. 2006, ARA&A, 44, 507
Yao, Y., Miller, A. A., Kulkarni, S. R., et al. 2019, ApJ, 886, 152
Yaron, O., & Gal-Yam, A. 2012, PASP, 124, 668
Zackay, B., Ofek, E. O., & Gal-Yam, A. 2016, ApJ, 830, 27